A Geometric Perspective on Diffusion Models

Defang Chen¹ Zhenyu Zhou¹ Jian-Ping Mei² Chunhua Shen¹ Chun Chen¹ Can Wang¹

¹Zhejiang University ²Zhejiang University of Technology

Abstract

Recent years have witnessed significant progress in developing efficient training and fast sampling approaches for diffusion models. A recent remarkable advancement is the use of stochastic differential equations (SDEs) to describe data perturbation and generative modeling in a unified mathematical framework. In this paper, we reveal several intriguing geometric structures of diffusion models and contribute a simple yet powerful interpretation to their sampling dynamics. Through carefully inspecting a popular variance-exploding SDE and its marginal-preserving ordinary differential equation (ODE) for sampling, we discover that the data distribution and the noise distribution are smoothly connected with an explicit, quasi-linear sampling trajectory, and another implicit denoising trajectory, which even converges faster in terms of visual quality. We also establish a theoretical relationship between the optimal ODE-based sampling and the classic mean-shift (mode-seeking) algorithm, with which we can characterize the asymptotic behavior of diffusion models and identify the score deviation. These new geometric observations enable us to improve previous sampling algorithms, re-examine latent interpolation, as well as re-explain the working principles of distillation-based fast sampling techniques.

1 Introduction

Diffusion models, or score-based generative models [SDWMG15, SE19, HJA20, SSK⁺21, KAAL22] have attracted growing attention and seen impressive success in various domains, including image [DN21, VKK21, RBL⁺22], video [HSG⁺22, BRL⁺23], audio [KPH⁺21, CZZ⁺21], and especially text-to-image generation [RDN⁺22, SCS⁺22, PJBM23]. Such models are essentially governed by a certain kind of stochastic differential equations (SDEs) that smooth data into noise in a forward process and then generate data from noise in a backward process [SSK⁺21].

Generally, the forward SDE is formulated as a spectrum of Gaussian *kernel density estimation* of the original data distribution with a specifically designed scaling factor and bandwidth [SSK+21]. As such, one can couple (theoretically infinite) data-noise pairs and train a noise-dependent neural network (*i.e.*, the diffusion model) to minimize the least square error for data reconstruction [KAAL22]. Once such a denoising model with sufficient capacity is well optimized, it will faithfully capture the score (gradient of the log-density *w.r.t.* the input) of the data density smoothed with various levels of noise [RS11, Vin11, AB14, KAAL22]. The generative ability is then emerged by simulating the (score-based) backward SDE with any numerical solvers [SSK+21]. Alternatively, we can simulate the corresponding ordinary differential equation (ODE) that preserves the same marginal distribution as the SDE [SSK+21, SME21, LZB+22, ZC23]. The deterministic ODE-based sampling gets rid of the stochasticity apart from the randomness of drawing initial samples, and thus makes the whole generative procedure more comprehensible and controllable [KAAL22]. However, more details about how diffusion models behave under this dense mathematical framework are still largely unknown.

In this paper, we provide a geometric perspective to deepen our understanding of diffusion models, especially the sampling dynamics. The state-of-the-art variance-exploding SDE [KAAL22] is taken as an example to reveal the underlying intriguing structures. Our empirical observations are illustrated

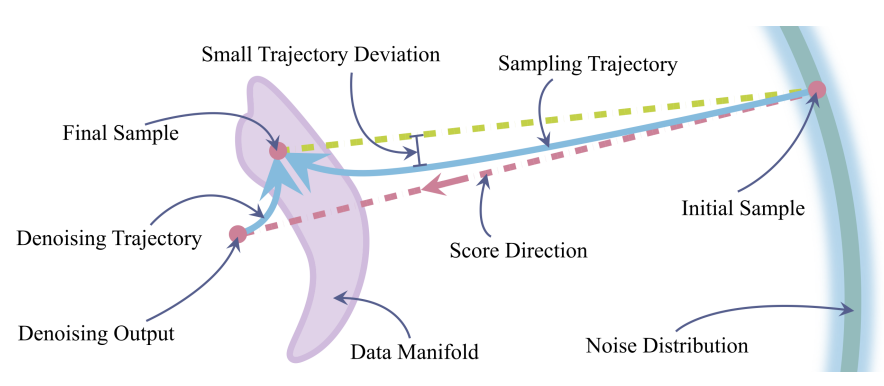


Figure 1: A geometric perspective of ODE-based sampling in diffusion models. An initial sample (from the noise distribution) starts from a big sphere and converges to its final sample (in the data manifold) along a smooth, quasi-linear sampling trajectory. Meanwhile, its denoising output lays in an implicit, smooth denoising trajectory starting from the approximate dataset mean. The denoising output is very close to the final sample and enjoys much faster convergence in terms of visual quality.

in Figure 1. Intuitively, given an initial sample from the noise distribution, the difference between its denoising output and its current position forms the scaled score for simulating the sampling trajectory. This explicit trajectory is almost straight such that the ODE simulation can be greatly accelerated at a modest cost of truncation error. Furthermore, the denoising output itself forms another implicit trajectory that starts near the final sample and quickly appears decent visual quality. These two simple and smooth trajectories depict the characters of ODE-based sampling and we further establish a theoretical relationship between the optimal ODE-based sampling and annealed mean shift to understand the asymptotic behavior of diffusion models. Additionally, we provide several applications to demonstrate the potential of our geometric perspective to reform existing practices of diffusion models, such as speeding up previous samplers, re-examining latent interpolation and re-interpreting distillation-based fast sampling techniques.

2 Score-Based Generative Models

We begin with a brief overview of the basic concepts in developing score-based generative models. To enable effective generative modeling, we are required to bridge the data distribution $p_d(\mathbf{x})$ with a non-informative tractable distribution $p_n(\mathbf{x})$. Nowadays, a prevailing and promising approach is score-based generative modeling [SSK+21, KAAL22, SCS+22, PJBM23], which can be formulated into a concise framework from the lens of *stochastic differential equations* (SDEs) [SSK+21, KAAL22]. With this powerful tool, the data perturbation is modeled as a continuous stochastic process $\{\mathbf{x}_t\}_{t=0}^T$:

$$d\mathbf{x} = \mathbf{f}(\mathbf{x}, t)dt + g(t)d\mathbf{w}_t, \qquad \mathbf{f}(\cdot, t) : \mathbb{R}^d \to \mathbb{R}^d, \quad g(\cdot) : \mathbb{R} \to \mathbb{R}, \tag{1}$$

where \mathbf{w}_t is the standard Wiener process; $\mathbf{f}(\cdot,t)$ and g(t) are drift and diffusion coefficients, respectively [Oks13]. We denote the distribution of \mathbf{x}_t as $p_t(\mathbf{x})$ and such an Itô SDE can smoothly transform the data distribution $p_0(\mathbf{x}) = p_d(\mathbf{x})$ to the (approximate) noise distribution $p_T(\mathbf{x}) \approx p_n(\mathbf{x})$ in a forward manner. By properly setting the coefficients, some established models referred to as variance-preserving (VP) and variance-exploding (VE) SDEs can be recovered [SE19, HJA20, SSK+21].

The reversal of Eq. (1) is another SDE that allows to synthesize data from noise in a backward manner [And82]. Remarkably, there exists a *probability flow ordinary differential equation* (PF-ODE) sharing the same marginal distribution $\{p_t(\mathbf{x})\}_{t=0}^T$ at each time step of the diffusion process:

$$d\mathbf{x} = \left[\mathbf{f}(\mathbf{x}, t)dt - \frac{1}{2}g(t)^{2}\nabla_{\mathbf{x}}\log p_{t}(\mathbf{x})\right]dt.$$
 (2)

The deterministic nature of ODE enjoys several benefits such as efficient sampling, unique encoding, and meaningful latent manipulations [SSK+21, KAAL22]. We thus choose Eq. (2) to analyze model behaviors throughout this paper. Simulating the above ODE requests having the *score function* $\nabla_{\mathbf{x}} \log p_t(\mathbf{x})$ in hand, which is typically estimated with the *denoising score matching* (DSM) criterion [Hyv05, Vin11, SE19]. From the perspective of *empirical Bayes* [Rob56, Efr11, SH19], there exists a

profound connection between DSM and *denoising autoencoder* (DAE) [VLBM08, AB14, KAAL22] (see Appendix B.1). Therefore, we can equivalently obtain the score function *at each noise level* by solving the corresponding least squares estimation:

$$\mathbb{E}_{\mathbf{x} \sim p_d} \mathbb{E}_{\mathbf{z} \sim \mathcal{N}(\mathbf{0}, \sigma_t^2 \mathbf{I})} \| r_{\boldsymbol{\theta}} \left(\hat{\mathbf{x}}; \sigma_t \right) - \mathbf{x} \|_2^2, \qquad \hat{\mathbf{x}} = \mathbf{x} + \mathbf{z}, \quad \sigma_t = \sqrt{\int_0^t g(\xi)^2 d\xi}. \tag{3}$$

The optimal estimator $r_{\theta}^{\star}(\hat{\mathbf{x}}; \sigma_t)$ equals to $\hat{\mathbf{x}} + \sigma_t^2 \nabla_{\hat{\mathbf{x}}} \log p_t(\hat{\mathbf{x}})$ as revealed in the literature [RS11, KAAL22]. Unless otherwise specified, we follow the configurations of VE SDEs with $\mathbf{f}(\mathbf{x},t) = \mathbf{0}$ and $g(t) = \sqrt{2t}$ [KAAL22, SDCS23]. In this case, $\sigma_t = t$, the perturbation kernel $p_t(\hat{\mathbf{x}}|\mathbf{x}) = \mathcal{N}(\hat{\mathbf{x}}; \mathbf{x}, t^2\mathbf{I})$, and the Parzen window density $p_t(\hat{\mathbf{x}}) = \int p_{\delta}(\mathbf{x})p_t(\hat{\mathbf{x}}|\mathbf{x})\mathrm{d}\mathbf{x}$ with $p_{\delta}(\mathbf{x})$ as the empirical data distribution. After training, we can leverage the empirical PF-ODE for sampling:

$$d\mathbf{x} = -\frac{r_{\boldsymbol{\theta}}(\mathbf{x};t) - \mathbf{x}}{t}dt.$$
 (4)

Specifically, we first draw $\hat{\mathbf{x}}_T \sim p_n(\mathbf{x}) = \mathcal{N}(\mathbf{0}, T^2\mathbf{I})$ and then numerically solve the ODE backwards with N steps to obtain a discrete sequence $\{\hat{\mathbf{x}}_s\}$ with $s \in \{s_0 = 0, s_1, \cdots, s_N = T\}$. The final sample $\hat{\mathbf{x}}_{s_0}$ is considered to approximately follow the data distribution $p_d(\mathbf{x})$.

3 Visualization of High Dimensional Trajectory

In this section, we present several viewpoints to inspect the trajectory of probability flow ODE in high-dimensional space. We follow the experimental settings of a recent and influential framework called EDMs [KAAL22]. Specifically, we focus on a forward VE SDE with $d\mathbf{x} = \sqrt{2t}\,d\mathbf{w}_t$ and its empirical ODE as Eq. (4) for sampling. We mostly take unconditional generation on the CIFAR-10 dataset as an example to demonstrate our observations. The conclusions also hold on other datasets (such as LSUN Cat, LSUN Bedroom) and other model settings (such as conditional generation, various network architectures). More results and implementation details are provided in Appendix A.

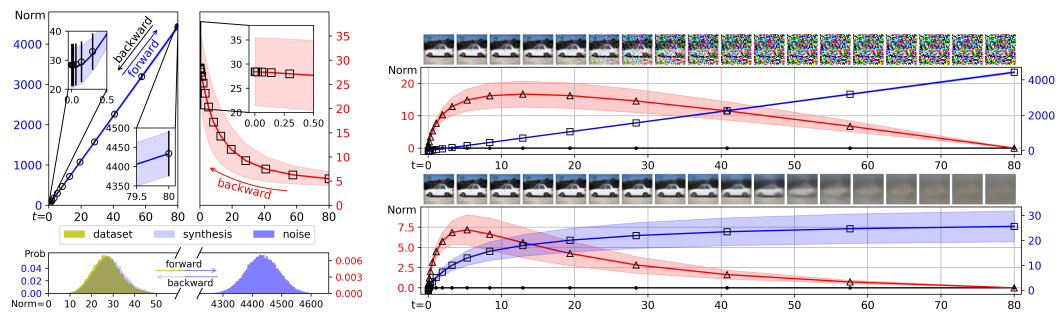
3.1 Magnitude Expansion/Shrinkage

As discussed in Section 2, the forward diffusion process is generally interpreted as a progressive smoothing from the data distribution to the noise distribution with a Gaussian kernel $p_t(\hat{\mathbf{x}}|\mathbf{x})$. In contrast, we further paraphrase it as the expansion of magnitude and manifold, which means that samples escape from the original *small-magnitude low-rank* manifold and settle into a *large-magnitude high-rank* manifold. The following proposition gives us a glimpse of the geometric structure in high dimensions:

Proposition 1. Given a high-dimensional vector $\mathbf{x} \in \mathbb{R}^d$ and an isotropic Gaussian noise $\mathbf{z} \sim \mathbb{N}\left(\mathbf{0}; \sigma^2 \mathbf{I}_d\right)$, $\sigma > 0$, we have $\mathbb{E} \|\mathbf{z}\|^2 = \sigma^2 d$, and with high probability, \mathbf{z} stays within a "thin shell": $\|\mathbf{z}\| = \sigma \sqrt{d} \pm O(1)$. Additionally, $\mathbb{E}\left[\|\mathbf{x} + \mathbf{z}\|^2 - \|\mathbf{x}\|^2\right] = \sigma^2 d$, $\lim_{d \to \infty} \mathbb{P}\left(\|\mathbf{x} + \mathbf{z}\| > \|\mathbf{x}\|\right) = 1$.

The proofs are provided in Appendix B.2. Proposition 1 implies that in the forward process, the squared magnitude of the noisy sample $\mathbf{x}+\mathbf{z}$ is expected to be larger than that of the original sample \mathbf{x} , and their magnitude gap becomes especially huge for the high-dimensional case $d\gg 1$ and severe noise case $\sigma\gg 0$. We can further conclude that asymptotically $(d\to\infty)$, the sample magnitude will expand with probability one and the isotropic Gaussian noise will distribute as a uniform distribution on the sphere, i.e., $\mathbf{z}\sim \mathcal{N}(\mathbf{0};\sigma^2\mathbf{I}_d)=\mathrm{Unif}(\sigma\sqrt{d}\,\mathbb{S}^{d-1})$, due to the concentration of measure [Ver18, SH19]. In practical generation, d is sufficiently large to make the above claim approximately correct. The low-rank data manifold is thus lifted to about d-1 rank sphere of radius $\sigma\sqrt{d}$ with a thin spherical shell of width O(1). Due to the marginal preserving property of PF-ODE [SSK+21], the backward process behaves in a magnitude shrinking fashion and the analysis is similar.

In Figure 2a, we track the magnitude (ℓ_2) of original data (the pixel values are re-scaled to [-1,1]) in the forward process and the magnitude of synthetic samples in the backward process. A clear trend is the sample magnitude expands in the forward diffusion process and shrinks in the backward sampling process, and they are well-matched thanks to the marginal preserving property. Furthermore, the isotropic Gaussian noise is distributed around the sphere of radius (about 4433 ± 57), which is significantly larger than the original data in magnitude (about 27 ± 7).



- (a) The statistics of magnitude.
- (b) Deviation in the sampling (top)/denoising (bottom) trajectories.

Figure 2: (a) The magnitude of samples in the forward process (blue curve), the backward process (black circle) and the denoising outputs (red curve). (b) The *trajectory deviation* (red curve) and the ℓ_2 distance between intermediate samples and the final sample in the trajectory (blue curve).

3.2 Geometric Shape of Sampling/Denoising Trajectory

Given an ODE in Eq. (4) linking the data distribution $p_d(\mathbf{x})$ and the noise distribution $p_n(\mathbf{x})$, we denote sampling trajectory as the discrete sequence $\{\hat{\mathbf{x}}_s\}_{s_N}^{s_0}$ with $s \in \{s_0 = 0, s_1, s_2, \cdots, s_N = T\}^1$, starting from $\hat{\mathbf{x}}_{s_N} \sim \mathcal{N}(\mathbf{0}, T^2\mathbf{I})$. We adopt symbol $d(\cdot, \cdot)$ to denote the ℓ_2 distance between two points, such as $d(\hat{\mathbf{x}}_s, \hat{\mathbf{x}}_{s_0})$, and the trajectory deviation from a point to the straight line passing through the initial and final points in the trajectory, such as $d(\hat{\mathbf{x}}_s, [\hat{\mathbf{x}}_{s_0}\hat{\mathbf{x}}_{s_N}])$. Additionally, we denote another important yet easy to be ignored sequence as $\{r_{\theta}(\hat{\mathbf{x}}_s, s)\}_{s_N}^{s_1}$ or simplified to $\{r_{\theta}(\hat{\mathbf{x}}_s)\}_{s_N}^{s_1}$ if no ambiguity, and designate it as denoising trajectory. A sampling trajectory and its associated denoising trajectory are provided in Figure 2b for illustration.

Proposition 2. The denoising output $r_{\theta}(\mathbf{x};t)$ reflects the prediction made by a single Euler step from any sample \mathbf{x} at any time towards t = 0 with Eq. (4).

Proof. The prediction of such an Euler step equals to $\mathbf{x} - (0 - t) \left(r_{\theta} \left(\mathbf{x}; t \right) - \mathbf{x} \right) / t = r_{\theta} \left(\mathbf{x}; t \right)$.

This property was previously stated as an intuitive evidence to advocate the use of Eq. (4) for sampling [KAAL22]. There, Karras *et al.* suspected that this ODE trajectory is approximately linear across most noise levels due to the slow change of denoising output, and verified it in the 1-dimensional situation. In contrast, we provide an in-depth analysis of the high-dimensional trajectory with real data, and reveal its connection to the classic mean-shift (mode seeking) algorithm [FH75, Che95, CM02].

Visualization. It is very challenging to visualize the whole sampling trajectory and denoising trajectory laying in high-dimensional space. In this paper, we are particularly interested in their geometric properties, and find that the trajectory structure exhibits a surprisingly simple form. Our observations, which have been confirmed by empirical evidence, are summarized and elaborated in the following paragraphs. The expectation quantities (such as distance, magnitude) in each discrete time step are estimated by averaging 50k generated samples.

Observation 1. The sampling trajectory is almost straight while the denoising trajectory is bent.

We develop an efficient visualization technique based on *trajectory deviation* to assess the linearity of trajectories. From Figure 2b, we can see that the deviation of sampling trajectory and denoising trajectory (red curve) gradually increases from t=80 to around t=10 or t=5, respectively, and then quickly decreases until reaching the final point. This implies that the initial point may be affected by all possible modes with a large influence at first, and become intensely attracted by its unique mode after a turning point. This phenomenon also supports the strategy of placing time intervals densely near the minimum timestamp yet sparsely near the maximum one [KAAL22, SDCS23]. However, based on the ratio of maximum deviation (such as $\max d(\hat{\mathbf{x}}_s, [\hat{\mathbf{x}}_{s_0}\hat{\mathbf{x}}_{s_N}])$) to the endpoint distance (such as $d(\hat{\mathbf{x}}_{s_0}, \hat{\mathbf{x}}_{s_N})$), the curvature of sampling trajectory is incredibly small (about $16/4428 \approx 0.0036$), while the curvature of denoising trajectory is relatively significant (about $7/26 \approx 0.27$).

¹The time horizon is divided with the formula $s_n = (s_1^{1/\rho} + \frac{n-1}{N-1}(s_N^{1/\rho} - s_1^{1/\rho}))^{\rho}$, where $s_1 = 0.002$, $s_N = 80$, $n \in [1, N]$ and $\rho = 7$ [KAAL22].

Another evidence for quasi-linearity of the sampling trajectory is from the aspect of angle deviation, which is calculated by the cosine between the backward ODE direction $-\frac{\mathrm{d}\mathbf{x}_t}{\mathrm{d}t}\big|_s$ and the direction pointing to the final point $(\hat{\mathbf{x}}_{s_0} - \hat{\mathbf{x}}_s)$ at discrete time s. We find that $\cos\left(-\frac{\mathrm{d}\mathbf{x}_t}{\mathrm{d}t}\big|_s, (\hat{\mathbf{x}}_{s_0} - \hat{\mathbf{x}}_s)\right)$ always stays in a narrow range from 0.98 to 1.00 (see Appendix A), which indicates that the angle deviation is extremely small and all backward ODE directions almost exactly point to the final point.

Observation 2. The generated samples on the sampling trajectory and denoising trajectory both move monotonically from the initial points toward their converged points in expectation, i.e., $\{\mathbb{E}\left[d(\hat{\mathbf{x}}_s,\hat{\mathbf{x}}_{s_0})\right]\}_{s_N}^{s_0}$ and $\{\mathbb{E}\left[d(r_{\theta}(\hat{\mathbf{x}}_s),r_{\theta}(\hat{\mathbf{x}}_{s_1}))\right]\}_{s_N}^{s_1}$ are monotone decreasing sequences.

This is inferred from the blue curves in Figure 2b. In fact, such behavior is expected for the sampling trajectory given its slight angle deviation. Since $\forall s, -\frac{d(\mathbf{x}_t, \hat{\mathbf{x}}_{s_0})}{dt}\big|_s \propto \cos\left((\hat{\mathbf{x}}_{s_0} - \hat{\mathbf{x}}_s), \frac{d\mathbf{x}_t}{dt}\big|_s\right) \approx -1$, the initial point will converge monotonically and rapidly by moving along the backward ODE direction, similar to the behavior of gradient descent algorithm in a well-behaved convex function.

The above two observations enable us to safely adopt large numerical Euler steps or higher-order ODE solvers without incurring much truncation error in most cases [KAAL22, LZB⁺22, ZC23].

Observation 3. The sampling trajectory converges to the data distribution in a monotone magnitude shrinking way. Conversely, the denoising trajectory converges to the data distribution in a monotone magnitude expanding way. Formally, we have $\{\mathbb{E}\|\hat{\mathbf{x}}_s\|_{s_N}^{s_0}\downarrow$ and $\{\mathbb{E}\|r_{\boldsymbol{\theta}}(\hat{\mathbf{x}}_s)\|_{s_N}^{s_1}\uparrow$.

Although generated samples converge monotonically, whether along the sampling trajectory or denoising trajectory (Observation 2), their magnitude behaves differently (Figure 2a). Geometrically, the initial noise distribution $p(\hat{\mathbf{x}}_{s_N})$ starts from a big sphere of radius $T\sqrt{d}$ and then anisotropically squashes its "radius" and twists the sample range into the exact data manifold. Meanwhile, the initial denoising output is an approximate *Dirac delta function* centering in the dataset mean vector \mathbf{x}_m , *i.e.*, $p(r_{\theta}(\hat{\mathbf{x}}_{s_N})) = \delta(\mathbf{x}_m)$ [KAAL22]. This Dirac delta function anisotropically expands its range until exactly matching the data manifold. The overall picture is illustrated in Figure 1.

4 Theoretical Connection to Mean Shift

Given a parametric diffusion model with the denoising output r_{θ} , the sampling trajectory is simulated by numerically solving Eq. (4), and meanwhile, an implicitly coupled denoising trajectory is formed as a by-product. Once such a model has converged, it will hopefully capture the underlying score at different levels of noise, i.e., $\forall \sigma_t, \ r_{\theta} \ (\hat{\mathbf{x}}; \sigma_t) \to r_{\theta}^{\star} \ (\hat{\mathbf{x}}; \sigma_t) \ [SSK^+21, KAAL22]$. We next derive the formula of optimal denoising output to analyze the asymptotic behavior of diffusion models.

Proposition 3. The optimal denoising output of Eq. (3) is a convex combination of the original data, where each weight is calculated based on the time-scaled and normalized ℓ_2 distance between $\hat{\mathbf{x}}$ and \mathbf{x}_i belonging to the dataset D:

$$r_{\boldsymbol{\theta}}^{\star}(\hat{\mathbf{x}}; \sigma_t) = \sum_{i} u_i \mathbf{x}_i = \sum_{i} \frac{\exp\left(-\|\hat{\mathbf{x}} - \mathbf{x}_i\|^2 / 2\sigma_t^2\right)}{\sum_{j} \exp\left(-\|\hat{\mathbf{x}} - \mathbf{x}_j\|^2 / 2\sigma_t^2\right)} \mathbf{x}_i, \quad \sum_{i} u_i = 1.$$
 (5)

The proof is provided in Appendix B.3. This equation appears to be highly similar to the classic non-parametric mean shift [FH75, Che95, CM02], and we provide a brief overview of it as follows.

Proposition 4. The mean-shift algorithm with a Gaussian kernel and bandwidth h iteratively moves a point \mathbf{x} along the mean-shift vector $m(\mathbf{x}) - \mathbf{x}$, i.e., $\mathbf{x} \leftarrow [m(\mathbf{x}) - \mathbf{x}] + \mathbf{x}$, towards the maximum increase in the Parzen window density $p(\hat{\mathbf{x}}) = \int p_{\delta}(\mathbf{x}) \mathcal{N}(\hat{\mathbf{x}}; \mathbf{x}, h^2 \mathbf{I}) d\mathbf{x}$, the mean vector is

$$\mathbf{m}\left(\mathbf{x},h\right) = \sum_{i} v_{i} \mathbf{x}_{i} = \sum_{i} \frac{\exp\left(-\|\mathbf{x} - \mathbf{x}_{i}\|^{2} / 2h^{2}\right)}{\sum_{j} \exp\left(-\|\mathbf{x} - \mathbf{x}_{j}\|^{2} / 2h^{2}\right)} \mathbf{x}_{i}, \quad \mathbf{x}_{i} \in \mathcal{D}, \quad \sum_{i} v_{i} = 1.$$
 (6)

From the interpretation of expectation-maximization (EM) algorithm, the above mean-shift iteration converges from almost any initial point with a generally linear convergence rate [CP07].

As a mode-seeking algorithm, mean shift has shown particularly successful in clustering [Che95], image segmentation [CM02] and video tracking [SBvdH05]. In fact, the ODE-based sampling is closely connected with *annealed mean shift*, or *multi-bandwidth mean shift* [SBvdH05], which was developed as a metaheuristic algorithm for global model-seeking. By treating the optimal denoising output in Eq. (5) as the mean vector in annealed mean-shift iterations, we have the following theorem:

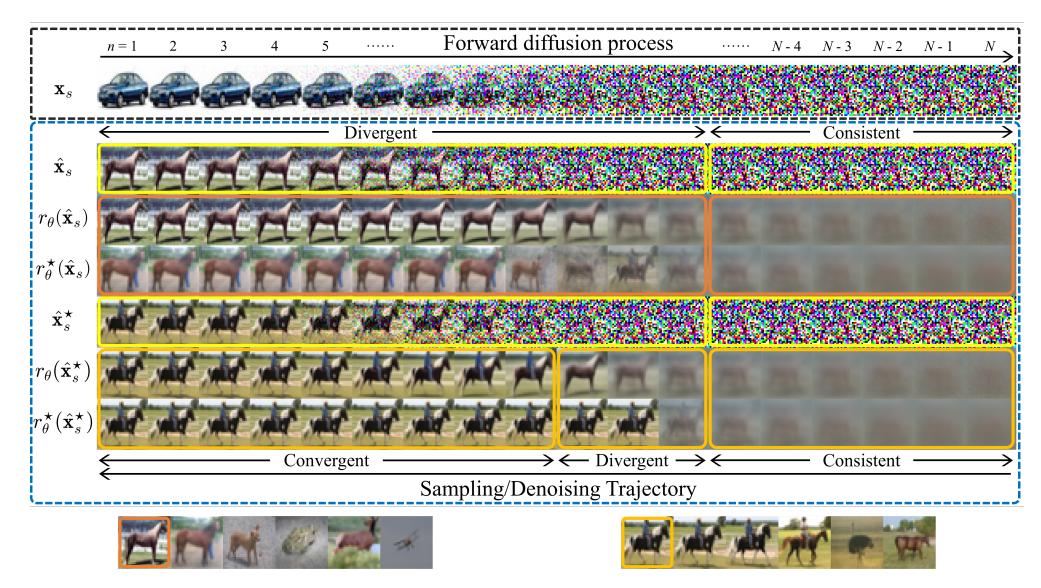


Figure 3: *Top*: We visualize a forward diffusion process of a randomly-selected image to obtain its encoding $\hat{\mathbf{x}}_{s_N}$ and simulate multiple trajectories starting from this encoding. *Bottom:* The k-nearest neighbors (k=5) of $r_{\theta}(\hat{\mathbf{x}}_{s_1})$ and $r_{\theta}^{\star}(\hat{\mathbf{x}}_{s_1}^{\star})$.

Theorem 1. Given an ODE $d\mathbf{x} = -\frac{r_{\theta}^{\star}(\mathbf{x};t) - \mathbf{x}}{t}dt$, one Euler step equals to a convex combination of the annealed mean-shift iteration and the current position.

Proof. Given a current sample $\hat{\mathbf{x}}_{s_{n+1}}$, $n \in [0, N-1]$, the prediction of an one-step Euler equals to

$$\hat{\mathbf{x}}_{s_{n}} = \hat{\mathbf{x}}_{s_{n+1}} - \frac{s_{n} - s_{n+1}}{s_{n+1}} \left(r_{\theta}^{\star} \left(\hat{\mathbf{x}}_{s_{n+1}}; s_{n+1} \right) - \hat{\mathbf{x}}_{s_{n+1}} \right)
= \frac{s_{n}}{s_{n+1}} \hat{\mathbf{x}}_{s_{n+1}} + \frac{s_{n+1} - s_{n}}{s_{n+1}} \mathbf{m} \left(\hat{\mathbf{x}}_{s_{n+1}}; s_{n+1} \right),$$
(7)

where we treat timestamp s_{n+1} in $r^*_{\theta}(\cdot)$ as the annealing-like bandwidth of Gaussian kernel in Eq. (6) and then replace it as one iteration of annealed mean shift $\mathbf{m}(\cdot)$ [SBvdH05].

The ratio of timestep $w(n)=(s_{n+1}-s_n)/s_{n+1}$ in Eq. (7) actually reflects our preference for annealed mean shift over sticking to the current position at s_{n+1} . Since the optimal denoising output, or annealed mean shift, starts with a spurious mode (dataset mean) and gradually converges towards a true mode over time, a reasonable choice is to progressively increase our emphasis on them, i.e., $\{w(n)\}_{s_{N-1}}^{s_0} \uparrow$. In this sense, various time-schedule functions (such as uniform, quadratic, polynomial [SE19, SME21, KAAL22]) essentially boil down to different weighting functions (see Appendix B.4). This interpretation inspires us to train a parametric neural network to adaptively select proper weights in sampling for better visual quality [KSPH21]. We leave it for future work.

Theorem 1 also implies that once diffusion models have converged to the optimum, all ODE trajectories will be uniquely determined and governed by a bandwidth-varying mean shift [CM02, SBvdH05]. In this case, the (forward) encoding process and (backward) decoding process only depend on the data distribution itself and a given noise distribution, regardless of model architectures or training algorithms. Such property was previously referred to as *uniquely identifiable encoding* and was empirically verified in [SSK+21], while we clearly characterize the optimum by drawing a connection with annealed mean shift, and thus reveal the asymptotic behavior of diffusion models.

5 Applications

5.1 Diagnosis of Score Deviation

We then simulate four new trajectories based on the optimal denoising output r_{θ}^{\star} to monitor the score deviation from the optimum: one is *optimal sampling trajectory* $\{\hat{\mathbf{x}}_{s}^{\star}\}_{s_{N}}^{s_{0}}$, where we generate samples

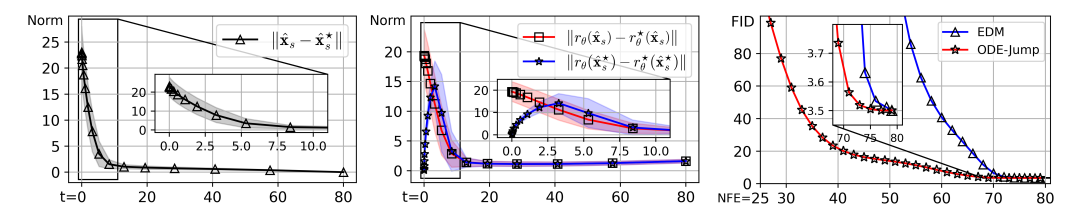


Figure 4: The score deviation in expectation (left and middle) and FID with different NFEs (right).



Figure 5: The synthesized images of our proposed ODE-Jump sampling (bottom) converge much faster than that of EDMs [KAAL22] (top) in terms of visual quality.

as $\{\hat{\mathbf{x}}_s\}_{s_N}^{s_0}$ but adopt r_{θ}^{\star} for score estimation, and other three are formed with the (optimal) denoising output and are designated as $\{r_{\theta}^{\star}(\hat{\mathbf{x}}_s)\}_{s_N}^{s_1}, \{r_{\theta}(\hat{\mathbf{x}}_s^{\star})\}_{s_N}^{s_1}, \{r_{\theta}^{\star}(\hat{\mathbf{x}}_s^{\star})\}_{s_N}^{s_1}$. We calculate the deviation of denoising output to quantify the score deviation in all time steps in terms of the ℓ_2 distance.

Observation 4. The learned score is well-matched to the optimal score in the large-noise region (from 80 to around 10), otherwise they may diverge or almost coincide depending on different regions.

In fact, our learned score has to moderately diverge from the optimum to guarantee the generative ability. Otherwise, the sampling reduces to annealed mean shift for mode-seeking, or simply replays the dataset. Empirically, score deviation in a small region is sufficient to bring forth such ability.

From $\{r_{\theta}(\hat{\mathbf{x}}_s^{\star})\}$, $\{r_{\theta}^{\star}(\hat{\mathbf{x}}_s^{\star})\}$ sequences in Figure 3 and the score deviation in Figure 4, we can clearly see that along the optimal sampling trajectory $\{\hat{\mathbf{x}}_s^{\star}\}$, the deviation between the learned score r_{θ} and the optimal score r_{θ}^{\star} behaves differently in three successive regions: the deviation starts off as almost negligible (about $10 < t \le 80$), gradually increases (about $3 < t \le 10$), and then drops down to a low level once again (about $0 \le t \le 3$). This phenomenon was also validated by a contemporaneous work [XTJ23] with a different viewpoint and measurement. We further observe that along the sampling trajectory $\{\hat{\mathbf{x}}_s\}$, this phenomenon disappears and the score deviation keeps increasing (see $\{r_{\theta}(\hat{\mathbf{x}}_s)\}$, $\{r_{\theta}^{\star}(\hat{\mathbf{x}}_s)\}$ sequences in Figure 3 and Figure 4). This indicates that our score-based model strives to explore novel regions. Additionally, the generated samples in trajectory are attracted to a real-data mode but do not fall into it, as supported by their k-nearest-neighbor samples in Figure 3.

5.2 Sampling with ODE-Jump

Observation 5. The (optimal) denoising trajectory converges faster than the (optimal) sampling trajectory in terms of visual quality.

This observation is inferred from the comparison of $\{\hat{\mathbf{x}}_s\}$ and $\{r_{\theta}(\hat{\mathbf{x}}_s)\}$, $\{\hat{\mathbf{x}}_s^{\star}\}$ and $\{r_{\theta}^{\star}(\hat{\mathbf{x}}_s)\}$ sequences in Figure 3, which inspires us to develop a new sampling algorithm named as *ODE-Jump* that directly jumps from *any* sample at *any* time in the sampling trajectory simulated by *any* ODE solver to the associated denoising trajectory, and returns the denoising output as the final synthesized image. This simple algorithm is highly flexible, extremely easy to implement, and converges considerably faster than the original ODE solver along the sampling trajectory. The quantitative comparison of Fréchet Inception Distance (FID [HRU⁺17]) *w.r.t.* the number of score function evaluations (NFEs) is provided in Figure 4 (right) and the visual comparison is provided in Figure 5.

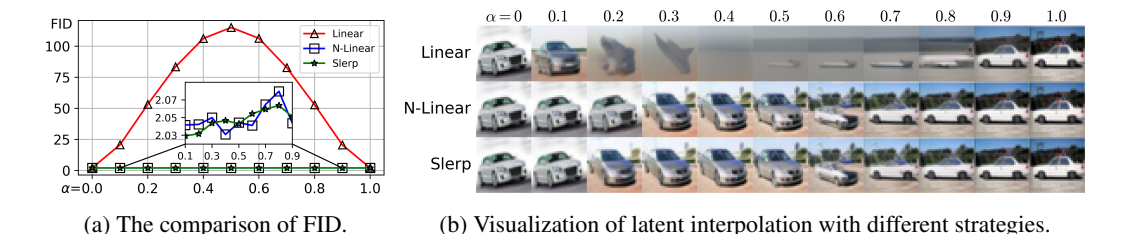


Figure 6: Linear latent interpolation results in blurry images, while a simple re-scaling trick greatly preserves the fine-grained image details and enables a smooth traversal among different modes.

5.3 In-Distribution Latent Interpolation

An attractive application of diffusion models is to achieve semantic image editing by manipulating latent representations [HJA20, SME21, SSK+21]. We then take *latent interpolation* as an example to reveal its working principle and the potential pitfalls in practice from a geometric viewpoint.

The training objective Eq. (3) for score estimation tells that given a noise level σ_t^2 , the denoiser is only trained with samples belonging to the distribution $p_t(\hat{\mathbf{x}})$. This important fact implies that for the latent encoding $\hat{\mathbf{x}}_{s_N} \sim \mathcal{N}(\mathbf{0}, T^2\mathbf{I})$, the denoiser performance is only guaranteed for the input approximately distributed in a sphere of radius $T\sqrt{d}$ (see Section 3.1). This geometric picture helps in understanding the conditions under which latent interpolation may fail.

Proposition 5. In high dimensions, linear interpolation [HJA20] shifts the latent distribution while spherical linear interpolation [SME21] asymptotically $(d \to \infty)$ maintains the latent distribution.

Given two independent latent encodings, $\hat{\mathbf{x}}_{s_N}^{(1)}$, $\hat{\mathbf{x}}_{s_N}^{(2)} \sim \mathcal{N}(\mathbf{0}, T^2\mathbf{I})$, they are almost orthogonal with the angle $\frac{1}{2}\pi + O_p(d^{-0.5})$ in high dimensions [HMN05, Ver18]. In this case, *linear interpolation* $\hat{\mathbf{x}}_{s_N}^{(\alpha)} = (1-\alpha)\hat{\mathbf{x}}_{s_N}^{(1)} + \alpha\hat{\mathbf{x}}_{s_N}^{(2)}$ quickly pushes the resulting encoding $\hat{\mathbf{x}}_{s_N}^{(\alpha)}$ away from the original distribution into a squashed sphere of radius $T\sqrt{d((1-\alpha)^2+\alpha^2)}$, which almost has no intersection with the original sphere. Our trained denoiser thus can not provide a reliable estimation for $r_{\theta}(\hat{\mathbf{x}}_{s_N}^{(\alpha)}, s_N)$ to derive the score direction, as shown in Figure 6. Another strategy named as *spherical linear interpolation* (slerp) [SME21, SSK+21, RDN+22, SDCS23] greatly alleviates (but is not free from) the squashing effect in high dimensions and thus stabilizes the synthesis quality of interpolated encodings. But it still suffers from distribution shift in low dimensional cases (see Appendix B.5).

Proposition 6. *In-distribution interpolation preserves the latent distribution under interpolation.*

In particular, for the Gaussian encoding $\hat{\mathbf{x}}_{s_N}$, there exists a variance-preserving interpolation $\hat{\mathbf{x}}_{s_N}^{(\lambda)} = \sqrt{(1-\lambda^2)}\hat{\mathbf{x}}_{s_N}^{(1)} + \lambda\hat{\mathbf{x}}_{s_N}^{(2)} \sim \mathcal{N}\left(\mathbf{0}, T^2\mathbf{I}\right)$ to prevent distribution shift. Since a uniform λ makes $\hat{\mathbf{x}}_{s_N}^{(\lambda)}$ largely biased to $\hat{\mathbf{x}}_{s_N}^{(1)}$, we derive λ by re-scaling other heuristic strategies to scatter the coefficient more evenly, such as the *normalized linear* (n-linear) interpolation $(\lambda = \alpha/\sqrt{\alpha^2 + (1-\alpha^2)})$ with uniformly sampled coefficient α . As shown in Figure 6, this simple re-scaling trick significantly boosts the visual quality compared with the original counterpart. Additionally, slerp behaves as $\lambda = \sin\alpha\frac{\pi}{2}$ in high dimensions due to $\psi \approx \frac{\pi}{2}$, and this coefficient was used in [DN21] for interpolation.

With the help of such an in-distribution interpolation, all interpolated encodings faithfully move along our trained ODE trajectory with a reliable denoising estimation for $r_{\theta}(\hat{\mathbf{x}}_{s_N}^{(\lambda)}, s_N)$. We further calculate the k-nearest neighbors of our generated images to the real data (see Appendix A), to demonstrate how different modes are smoothly traversed in this process $\hat{\mathbf{x}}_{s_N} \to \hat{\mathbf{x}}_{s_N}^{\lambda} \to \hat{\mathbf{x}}_{s_0}^{\lambda}$.

5.4 Rethinking Distillation-Based Fast Sampling Techniques

A learned score-based model with a specified ODE solver fully determine the sampling trajectory and the denoising trajectory. From our geometric observations, many distillation-based fast sampling techniques can be re-interpreted as different ways to *linearize* the original sampling trajectory at several discrete time steps. Recently, *consistency distillation* (CD) [SDCS23] and TRACT [BAL⁺23] begin to rely on the denoising trajectory to guide the score fine-tuning and thus enable fast sampling.

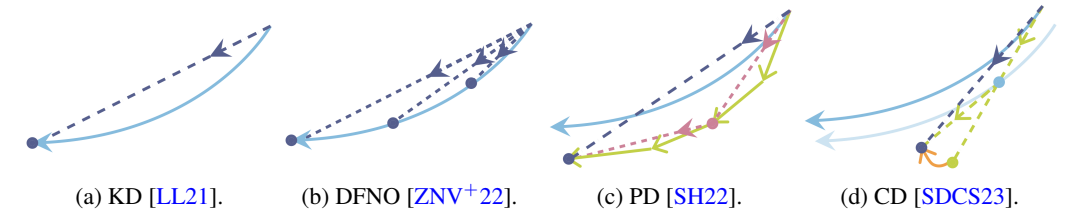


Figure 7: The comparison of distillation-based techniques. The *offline* techniques first simulate a long ODE trajectory with the teacher score and then make the student score points to the final point (KD [LL21]) or also include intermediate points on the trajectory (DFNO [ZNV+22]). The *online* techniques iteratively fine-tune the student prediction to align with the target simulated by a few-step teacher model along the sampling trajectory (PD [SH22]) or the denoising trajectory (CD [SDCS23]).

The slow sampling speed is a major bottleneck of score-based generative models. To address this issue, one possible solution is to explicitly straighten the ODE trajectory with knowledge distillation [LL21, SH22, ZNV+22, SDCS23]. They optimize a new student score model (r_{θ}) to align with the prediction of a pre-trained and fixed teacher score model (r_{ϕ}) . Empirically, these learning-based approaches can achieve decent synthesis quality with a significantly fewer NFE (\approx 1) compared to those ODE solver-based approaches [LZB+22, ZC23, SDCS23]. In Figure 7, we draw a sketch to highlight the difference of typical examples. The rationale behind these approaches is that with the pre-defined teacher sampling trajectory and its backward ODE simulation to obtain $\mathcal{T}_{\phi}(\cdot)$, we can adjust the student sampling direction by making the initial point directly point to the final point. To achieve this goal, new noise-target pairs are built in an online [SH22, SDCS23, BAL+23] or offline fashion [LL21, ZNV+22]. We present the training objective of CD as follows

$$\mathbb{E}_{\mathbf{x} \sim p_d} \mathbb{E}_{\mathbf{z} \sim \mathcal{N}(\mathbf{0}, s_{n+1}^2 \mathbf{I})} \| r_{\boldsymbol{\theta}} \left(\hat{\mathbf{x}}; s_{n+1} \right) - r_{\boldsymbol{\theta}^-} \left(\mathcal{T}_{\boldsymbol{\phi}} \left(\hat{\mathbf{x}} \right); s_n \right) \|_2^2, \quad \hat{\mathbf{x}} = \mathbf{x} + \mathbf{z}, \tag{8}$$

where $\mathfrak{T}_{\phi}\left(\hat{\mathbf{x}}\right)$ is implemented as an one-step Euler: $\hat{\mathbf{x}} - \frac{(s_n - s_{n+1})}{s_{n+1}} \left(r_{\phi}\left(\hat{\mathbf{x}}; s_{n+1}\right) - \hat{\mathbf{x}}\right)$. CD follows the time schedule of EDMs (see Section 3.2) [KAAL22], aside from removing the s_0 , and adopts pre-trained EDMs to initialize the student model. $\boldsymbol{\theta}^-$ is the exponential moving average (EMA) of $\boldsymbol{\theta}$.

Based on our geometric observations, we then provide an intuitive interpretation of the training objective Eq. (8). (1) The role of $\mathcal{T}_{\phi}(\hat{\mathbf{x}})$ is to locate the sampling trajectory passing a given noisy sample $\hat{\mathbf{x}}$ and make one numerical step along the trajectory to move $\hat{\mathbf{x}}$ towards its converged point. (2) $r_{\theta^-}(\cdot)$ further projects $\mathcal{T}_{\phi}(\hat{\mathbf{x}})$ into the corresponding denoising trajectory with the step size s_n . It is closer to the converged point, compared with the denoising output of $\hat{\mathbf{x}}$ with the step size s_{n+1} (see Observation 2 and Figure 7). (3) The student denoising output $r_{\theta}(\cdot)$ is then shifted to match its underlying target $r_{\theta^-}(\cdot)$ in the denoising trajectory. By iteratively fine-tuning denoising outputs until convergence, the student model is hopefully endowed with the ability to perform few-step sampling from those trained discrete time steps, and thus achieves excellent performance in practice [SDCS23].

6 Conclusion and Future Work

In this paper, we present a geometric perspective on (variance-exploding) diffusion models, aiming for a fundamental grasp of their sampling dynamics in a simple and intuitive way. We find that intriguingly, the data distribution and the noise distribution are smoothly bridged by a quasi-linear sampling trajectory, and another implicit denoising trajectory allowing faster convergence in terms of visual quality. We further characterize the asymptotic behavior of diffusion models by formulating a theoretical relationship between the optimal ODE-based sampling and the anneal mean-shift (global mode-seeking) algorithm. Additionally, some preliminary applications implied by our brand new geometric perspective are provided. We hope our theoretical understanding and empirical observations help to better harness the power of score/diffusion-based generative models and facilitate more rapid development in efficient training and fast sampling techniques.

One limitation is that our current observations are not fully underpinned by theoretical results, and thus require further investigation. In fact, the intensively used ODE-based sampling behaves as a typical non-autonomous non-linear system [Kha02], which offers a potential approach to analyze the (asymptotic) stability of diffusion models with tools from control theory.

References

- [AB14] Guillaume Alain and Yoshua Bengio. What regularized auto-encoders learn from the data-generating distribution. *Journal of Machine Learning Research*, 15(1):3563–3593, 2014.
- [And82] Brian DO Anderson. Reverse-time diffusion equation models. *Stochastic Processes and their Applications*, 12(3):313–326, 1982.
- [BAL⁺23] David Berthelot, Arnaud Autef, Jierui Lin, Dian Ang Yap, Shuangfei Zhai, Siyuan Hu, Daniel Zheng, Walter Talbot, and Eric Gu. Tract: Denoising diffusion models with transitive closure time-distillation. *arXiv preprint arXiv:2303.04248*, 2023.
- [BRL⁺23] Andreas Blattmann, Robin Rombach, Huan Ling, Tim Dockhorn, Seung Wook Kim, Sanja Fidler, and Karsten Kreis. Align your latents: High-resolution video synthesis with latent diffusion models. In *Proceedings of the IEEE/CVF Conference on Computer Vision and Pattern Recognition*, 2023.
 - [Che95] Yizong Cheng. Mean shift, mode seeking, and clustering. *IEEE Transactions on Pattern Analysis and Machine Intelligence*, 17(8):790–799, 1995.
 - [CM02] Dorin Comaniciu and Peter Meer. Mean shift: A robust approach toward feature space analysis. *IEEE Transactions on Pattern Analysis and Machine Intelligence*, 24(5):603–619, 2002.
 - [CP07] Miguel A Carreira-Perpinan. Gaussian mean-shift is an em algorithm. *IEEE Transactions on Pattern Analysis and Machine Intelligence*, 29(5):767–776, 2007.
- [CZZ⁺21] Nanxin Chen, Yu Zhang, Heiga Zen, Ron J. Weiss, Mohammad Norouzi, and William Chan. Wavegrad: Estimating gradients for waveform generation. In *International Conference on Learning Representations*, 2021.
 - [DN21] Prafulla Dhariwal and Alex Nichol. Diffusion models beat gans on image synthesis. In *Advances in Neural Information Processing Systems*, 2021.
 - [Efr10] Bradley Efron. Large-scale inference: empirical Bayes methods for estimation, testing, and prediction. Cambridge University Press, 2010.
 - [Efr11] Bradley Efron. Tweedie's formula and selection bias. *Journal of the American Statistical Association*, 106(496):1602–1614, 2011.
 - [EH16] Bradley Efron and Trevor Hastie. *Computer age statistical inference: algorithms, evidence, and data science.* Cambridge University Press, 2016.
 - [FH75] Keinosuke Fukunaga and Larry Hostetler. The estimation of the gradient of a density function, with applications in pattern recognition. *IEEE Transactions on information theory*, 21(1):32–40, 1975.
 - [HJA20] Jonathan Ho, Ajay Jain, and Pieter Abbeel. Denoising diffusion probabilistic models. In *Advances in Neural Information Processing Systems*, 2020.
- [HMN05] Peter Hall, James Stephen Marron, and Amnon Neeman. Geometric representation of high dimension, low sample size data. *Journal of the Royal Statistical Society: Series B (Statistical Methodology)*, 67(3):427–444, 2005.
- [HRU⁺17] Martin Heusel, Hubert Ramsauer, Thomas Unterthiner, Bernhard Nessler, and Sepp Hochreiter. GANs trained by a two time-scale update rule converge to a local Nash equilibrium. In *Advances in Neural Information Processing Systems*, pages 6626–6637, 2017.
- [HSG⁺22] Jonathan Ho, Tim Salimans, Alexey A. Gritsenko, William Chan, Mohammad Norouzi, and David J. Fleet. Video diffusion models. In *ICLR Workshop on Deep Generative Models for Highly Structured Data*, 2022.
 - [Hyv05] Aapo Hyvärinen. Estimation of non-normalized statistical models by score matching. *Journal of Machine Learning Research*, 6:695–709, 2005.
- [KAAL22] Tero Karras, Miika Aittala, Timo Aila, and Samuli Laine. Elucidating the design space of diffusion-based generative models. In Advances in Neural Information Processing Systems, 2022.
 - [KH09] Alex Krizhevsky and Geoffrey Hinton. Learning multiple layers of features from tiny images. *Technical Report*, 2009.

- [Kha02] Hassan K Khalil. Nonlinear systems third edition. Patience Hall, 115, 2002.
- [KPH⁺21] Zhifeng Kong, Wei Ping, Jiaji Huang, Kexin Zhao, and Bryan Catanzaro. Diffwave: A versatile diffusion model for audio synthesis. In *International Conference on Learning Representations*, 2021.
- [KSPH21] Diederik P Kingma, Tim Salimans, Ben Poole, and Jonathan Ho. Variational diffusion models. In *Advances in Neural Information Processing Systems*, 2021.
 - [LL21] Eric Luhman and Troy Luhman. Knowledge distillation in iterative generative models for improved sampling speed. *arXiv preprint arXiv:2101.02388*, 2021.
- [LZB⁺22] Cheng Lu, Yuhao Zhou, Fan Bao, Jianfei Chen, Chongxuan Li, and Jun Zhu. Dpm-solver: A fast ode solver for diffusion probabilistic model sampling in around 10 steps. In *Advances in Neural Information Processing Systems*, 2022.
 - [Mor83] Carl N. Morris. Parametric empirical bayes inference: theory and applications. *Journal of the American Statistical Association*, 78(381):47–55, 1983.
 - [Oks13] Bernt Oksendal. Stochastic differential equations: an introduction with applications. Springer Science & Business Media, 2013.
- [PJBM23] Ben Poole, Ajay Jain, Jonathan T Barron, and Ben Mildenhall. Dreamfusion: Text-to-3d using 2d diffusion. In *International Conference on Learning Representations*, 2023.
- [RBL⁺22] Robin Rombach, Andreas Blattmann, Dominik Lorenz, Patrick Esser, and Björn Ommer. High-resolution image synthesis with latent diffusion models. In *Proceedings of the IEEE/CVF Conference on Computer Vision and Pattern Recognition*, pages 10684–10695, 2022.
- [RDN⁺22] Aditya Ramesh, Prafulla Dhariwal, Alex Nichol, Casey Chu, and Mark Chen. Hierarchical text-conditional image generation with clip latents. *arXiv* preprint *arXiv*:2204.06125, 2022.
- [RDS⁺15] Olga Russakovsky, Jia Deng, Hao Su, Jonathan Krause, Sanjeev Satheesh, Sean Ma, Zhiheng Huang, Andrej Karpathy, Aditya Khosla, Michael S. Bernstein, Alexander C. Berg, and Fei-Fei Li. Imagenet large scale visual recognition challenge. *International Journal of Computer Vision*, 115(3):211–252, 2015.
 - [Rob56] Herbert E. Robbins. An empirical bayes approach to statistics. In *Proceedings of the Third Berkeley Symposium on Mathematical Statistics and Probability*, 1956.
 - [RS11] Martin Raphan and Eero P Simoncelli. Least squares estimation without priors or supervision. *Neural Computation*, 23(2):374–420, 2011.
- [SBvdH05] Chunhua Shen, Michael J. Brooks, and Anton van den Hengel. Fast global kernel density mode seeking with application to localisation and tracking. In *International Conference on Computer Vision*, pages 1516–1523, 2005.
- [SCS⁺22] Chitwan Saharia, William Chan, Saurabh Saxena, Lala Li, Jay Whang, Emily L Denton, Kamyar Ghasemipour, Raphael Gontijo Lopes, Burcu Karagol Ayan, Tim Salimans, et al. Photorealistic text-to-image diffusion models with deep language understanding. In *Advances in Neural Information Processing Systems*, pages 36479–36494, 2022.
- [SDCS23] Yang Song, Prafulla Dhariwal, Mark Chen, and Ilya Sutskever. Consistency models. In *International Conference on Machine learning*, 2023.
- [SDWMG15] Jascha Sohl-Dickstein, Eric Weiss, Niru Maheswaranathan, and Surya Ganguli. Deep unsupervised learning using nonequilibrium thermodynamics. In *International Conference on Machine Learning*, pages 2256–2265, 2015.
 - [SE19] Yang Song and Stefano Ermon. Generative modeling by estimating gradients of the data distribution. In *Advances in Neural Information Processing Systems*, 2019.
 - [SH19] Saeed Saremi and Aapo Hyvärinen. Neural empirical bayes. *Journal of Machine Learning Research*, 20:181:1–181:23, 2019.
 - [SH22] Tim Salimans and Jonathan Ho. Progressive distillation for fast sampling of diffusion models. In *International Conference on Learning Representations*, 2022.
 - [SME21] Jiaming Song, Chenlin Meng, and Stefano Ermon. Denoising diffusion implicit models. In *International Conference on Learning Representations*, 2021.

- [SSK⁺21] Yang Song, Jascha Sohl-Dickstein, Diederik P. Kingma, Abhishek Kumar, Stefano Ermon, and Ben Poole. Score-based generative modeling through stochastic differential equations. In *International Conference on Learning Representations*, 2021.
 - [Ver18] Roman Vershynin. *High-dimensional probability: An introduction with applications in data science*, volume 47. Cambridge university press, 2018.
 - [Vin11] Pascal Vincent. A connection between score matching and denoising autoencoders. *Neural Computation*, 23(7):1661–1674, 2011.
- [VKK21] Arash Vahdat, Karsten Kreis, and Jan Kautz. Score-based generative modeling in latent space. In *Advances in Neural Information Processing Systems*, 2021.
- [VLBM08] Pascal Vincent, Hugo Larochelle, Yoshua Bengio, and Pierre-Antoine Manzagol. Extracting and composing robust features with denoising autoencoders. In *International Conference on Machine learning*, pages 1096–1103, 2008.
 - [XTJ23] Yilun Xu, Shangyuan Tong, and Tommi Jaakkola. Stable target field for reduced variance score estimation in diffusion models. *arXiv preprint arXiv:2302.00670*, 2023.
- [YSZ⁺15] Fisher Yu, Ari Seff, Yinda Zhang, Shuran Song, Thomas Funkhouser, and Jianxiong Xiao. Lsun: Construction of a large-scale image dataset using deep learning with humans in the loop. *arXiv preprint arXiv:1506.03365*, 2015.
 - [ZC23] Qinsheng Zhang and Yongxin Chen. Fast sampling of diffusion models with exponential integrator. In *International Conference on Learning Representations*, 2023.
- [ZNV⁺22] Hongkai Zheng, Weili Nie, Arash Vahdat, Kamyar Azizzadenesheli, and Anima Anandkumar. Fast sampling of diffusion models via operator learning. *arXiv* preprint *arXiv*:2211.13449, 2022.

A Additional Experimental Details

A.1 Experimental Settings

Unless otherwise specified, we follow the configurations of VE SDEs with $\mathbf{f}(\mathbf{x},t) = \mathbf{0}$ and $g(t) = \sqrt{2t}$ [KAAL22, SDCS23]. In this case, the forward VE SDE is $d\mathbf{x} = \sqrt{2t} \, d\mathbf{w}_t$, and the empirical probability flow ODE is $d\mathbf{x} = -\frac{r_{\theta}(\mathbf{x};t) - \mathbf{x}}{t} dt$. The default ODE sampler is Heun's 2^{nd} order method. The time horizon is divided with the formula $s_n = (s_1^{1/\rho} + \frac{n-1}{N-1}(s_N^{1/\rho} - s_1^{1/\rho}))^{\rho}$, where $s_1 = 0.002$, $s_N = 80$, $n \in [1, N]$ and $s_0 = 0$, $\rho = 7$ [KAAL22].

- For experiments on CIFAR- 10^2 [KH09] (32×32), we adopt the official implementation and pre-trained checkpoints³ of EDMs [KAAL22] (N=18, NFE = 35).
- For experiments on LSUN Bedroom (256×256), LSUN Cat⁴ [YSZ⁺15] (256×256), and ImageNet-64⁵ [RDS⁺15] (64×64), we adopt the re-implementation and pre-trained checkpoints⁶ from consistency models [SDCS23] (N = 40, NFE = 79).

The experimental results provided in Section A.2 and A.3 confirm that the conclusions in the main submission still hold on other datasets (such as LSUN Cat, LSUN Bedroom) and other model settings (such as conditional generation, various network architectures). We also provide the preliminary results on VP-SDE in Section A.4. The experiments are conducted on 8 NVIDIA A100 GPUs.

A.2 More Results on the VE-SDE

In the main submission, we conduct unconditional generation with the checkpoint⁷ of the DDPM++ architecture. Under this experimental setup, we provide more results in this section, including:

- Sampling with ODE-Jump: As shown in Figure 8 and 9, our proposed ODE-Jump sampling converges significantly faster than EDM in terms of FID. Additionally, we observe that in a few cases (such as LSUN Cat in Figure 8), the final point of the sampling trajectory does not obtain the best FID, and meanwhile the score deviation of the point achieving minimum FID is relatively larger. This implies the model probably fails to learn a good score direction at that point and thus incurs the increase of FID thereafter. We further provide more visual comparison results between the EDM and ODE-Jump sampling in Figure 11 to 15 and their detailed counterparts in Figure 12 to 16.
- Angle Deviation: The results are provided in Figure 10;
- Diagnosis of Score Deviation: Besides Figure 3 in the main submission, we also observe that there exists a few cases where $\{r^{\star}_{\theta}(\hat{\mathbf{x}}_s)\}$ and $\{r^{\star}_{\theta}(\hat{\mathbf{x}}_s^{\star})\}$ almost share the same final sample, as shown in Figure 18. In this case, the score deviation is relatively small such that for the final sample of the denoising trajectory, its nearest neighbor to the image in the dataset is exactly the final sample of the corresponding optimal trajectory.
- *Latent Interpolation:* The k-nearest neighbors of the generated images in Figure 6 are provided in Figure 17 and the interpolation results on LSUN Cat are provided in Figure 19.
- Trajectory Shape on Other Datasets: The results are provided in Figure 20 and 21. Similar to Figure 2a, we track the magnitude of original data in the forward SDE process at 500 time steps uniformly distributed in [0, 80] and we track the magnitude of synthesized samples in the backward ODE process, starting from 50k randomly-sampled noise. We calculate the means and standard deviations at each time step, and plot them as circle mark and short black line, respectively, in Figure 20a and 21a. Additionally, we find that the magnitude shift happens in the last few time steps (see Figure 20a and 21a), unlike the case in Figure 2a

²https://www.cs.toronto.edu/~kriz/cifar.html

³https://nvlabs-fi-cdn.nvidia.com/edm (Creative Commons Attribution-NonCommercial Share-Alike 4.0 International License)

⁴https://www.yf.io/p/lsun

⁵https://www.image-net.org/index.php

⁶https://github.com/openai/consistency_models (MIT License)

https://nvlabs-fi-cdn.nvidia.com/edm/pretrained/edm-cifar10-32x32-uncond-vp.pkl

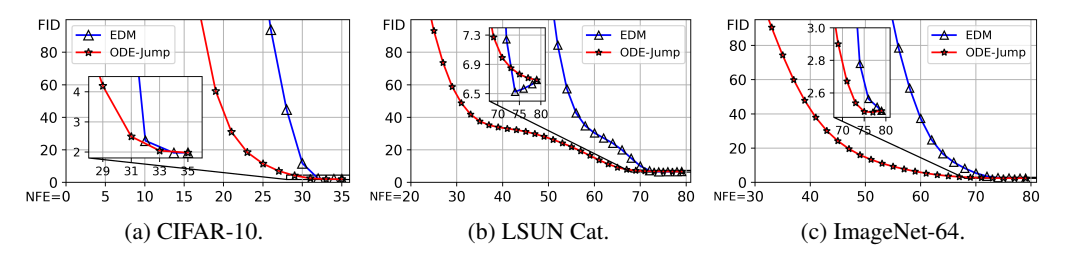


Figure 8: We calculate FIDs along the sampling trajectory (EDM [KAAL22]) and the denoising trajectory (ODE-Jump) with different NFEs. Our proposed ODE-Jump sampling converges significantly faster than EDM in terms of the FID.

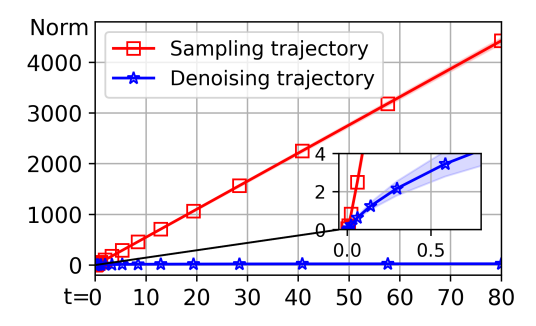


Figure 9: We compare the blue curves in Figure 2b, and find that the ℓ_2 distance between the intermediate sample and the final sample in the denoising trajectory is always smaller than that of the sampling trajectory, which supports the fast convergence of the denoising trajectory.

where the two distributions are highly aligned. In Figure 20b and 21b, we visualize the deviation in the sampling trajectory and the denoising trajectory as Figure 2b. A sampling trajectory and its associated denoising trajectory are also provided for illustration.

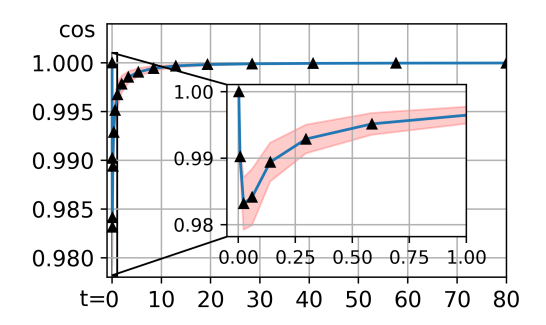


Figure 10: The angle deviation in the sampling trajectory is calculated by the cosine between the backward ODE direction $-\frac{d\mathbf{x}_t}{dt}\big|_s$ and the direction pointing to the final point $(\hat{\mathbf{x}}_{s_0} - \hat{\mathbf{x}}_s)$ at discrete time s. The angle deviation always stays in a narrow range (from about 0.98 to 1.00).

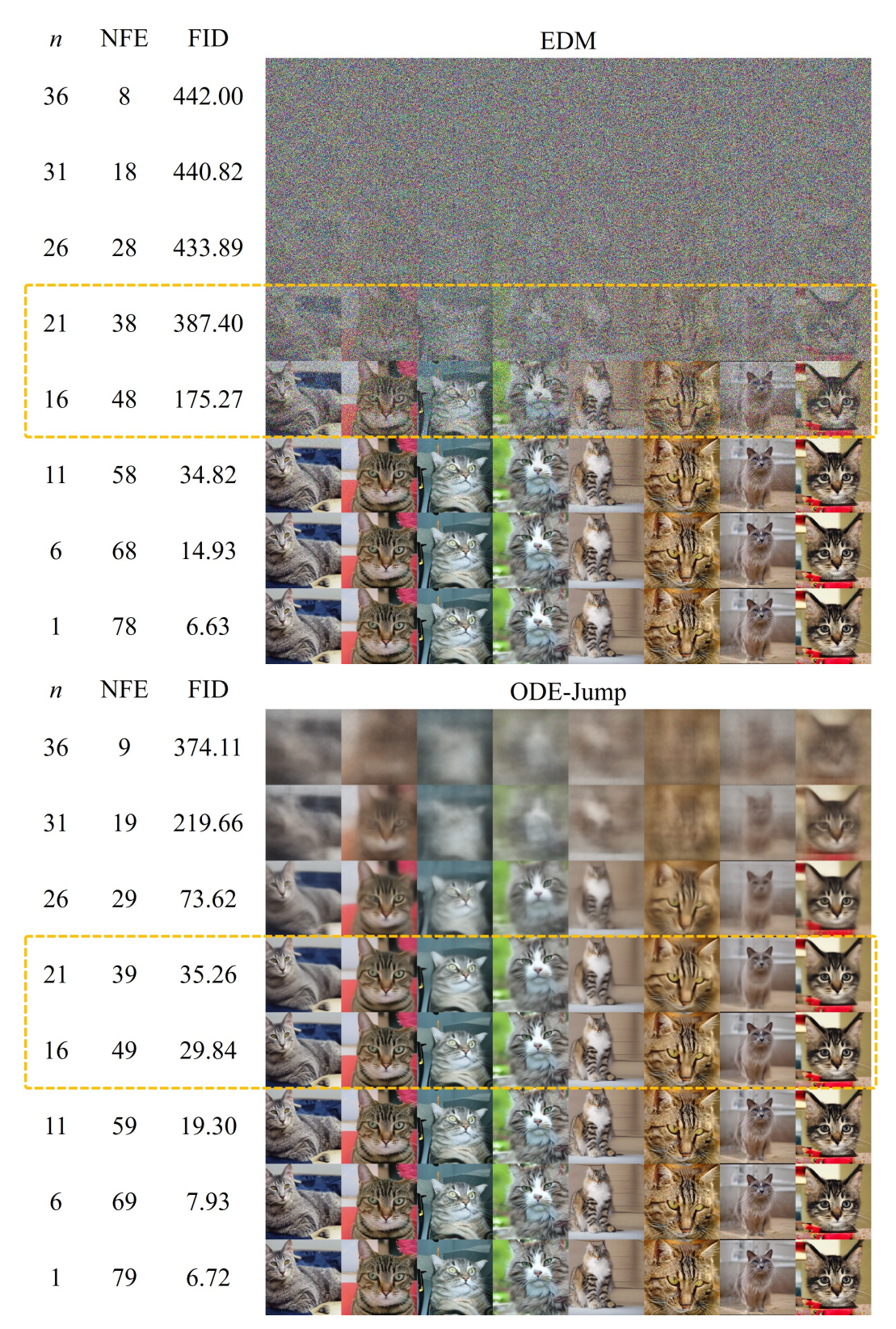


Figure 11: The visual comparison of EDM and ODE-Jump on LSUN Cat.

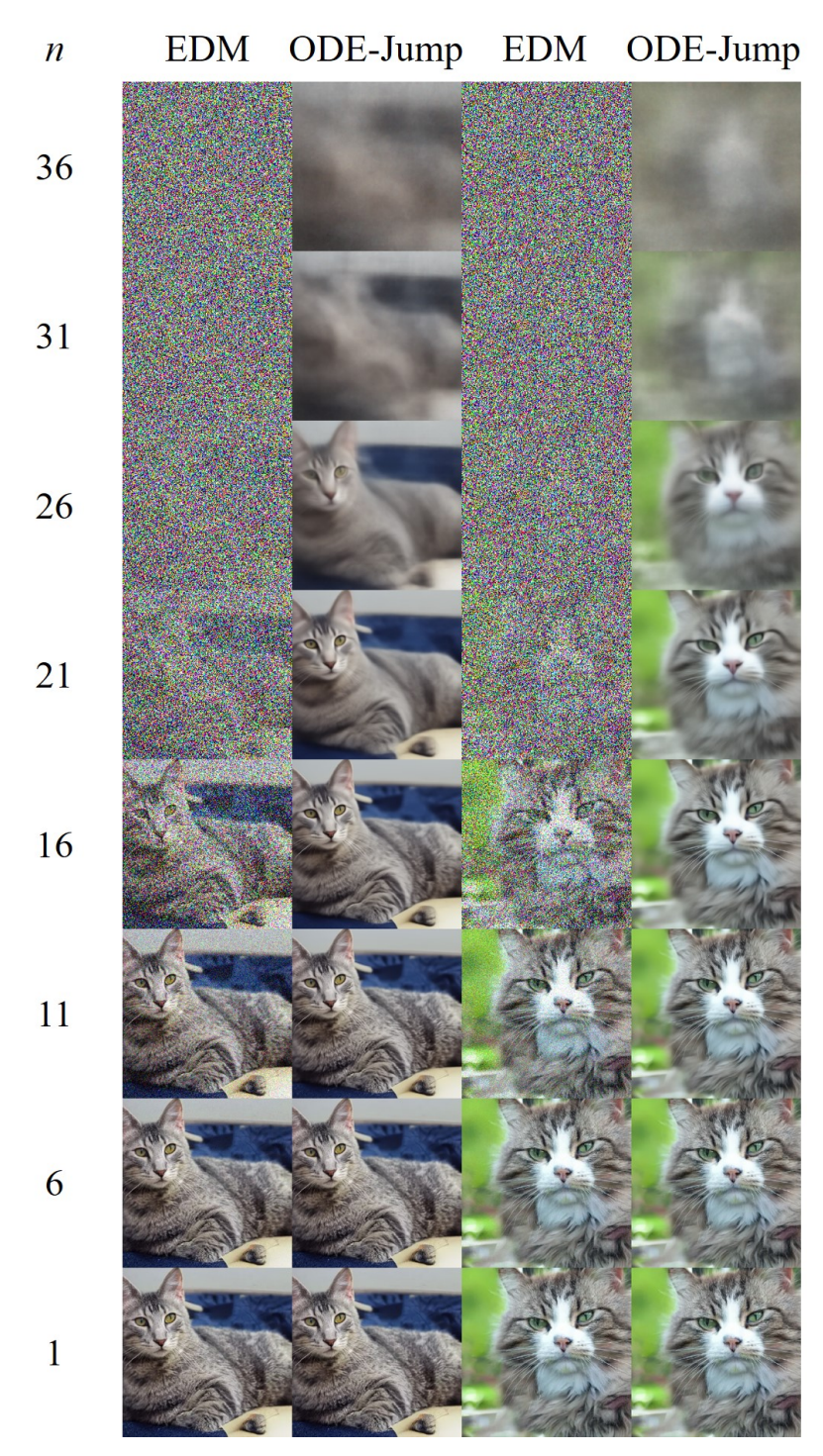


Figure 12: The visual comparison of EDM and ODE-Jump on LSUN Cat (detailed version).

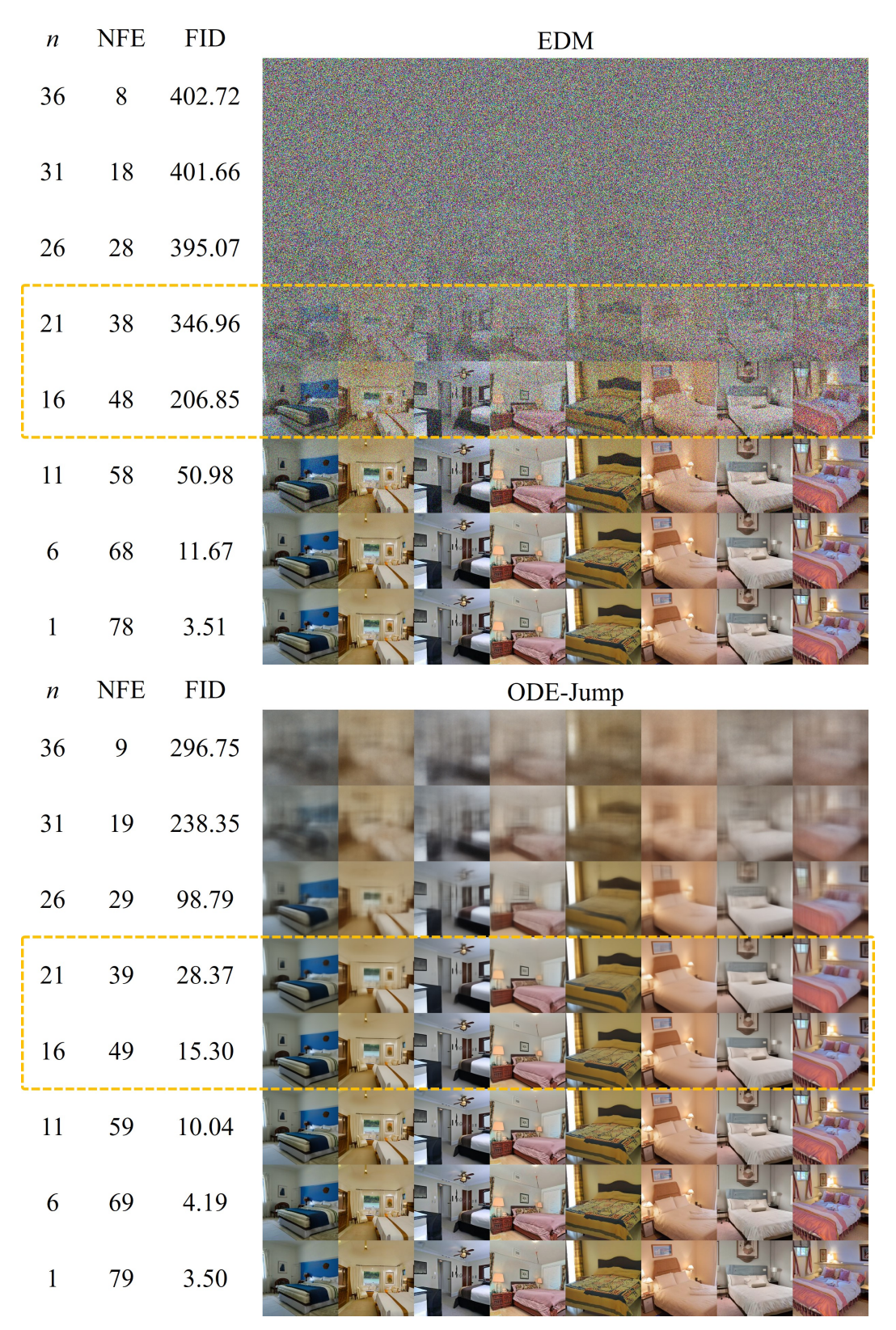


Figure 13: The visual comparison of EDM and ODE-Jump on LSUN Bedroom.

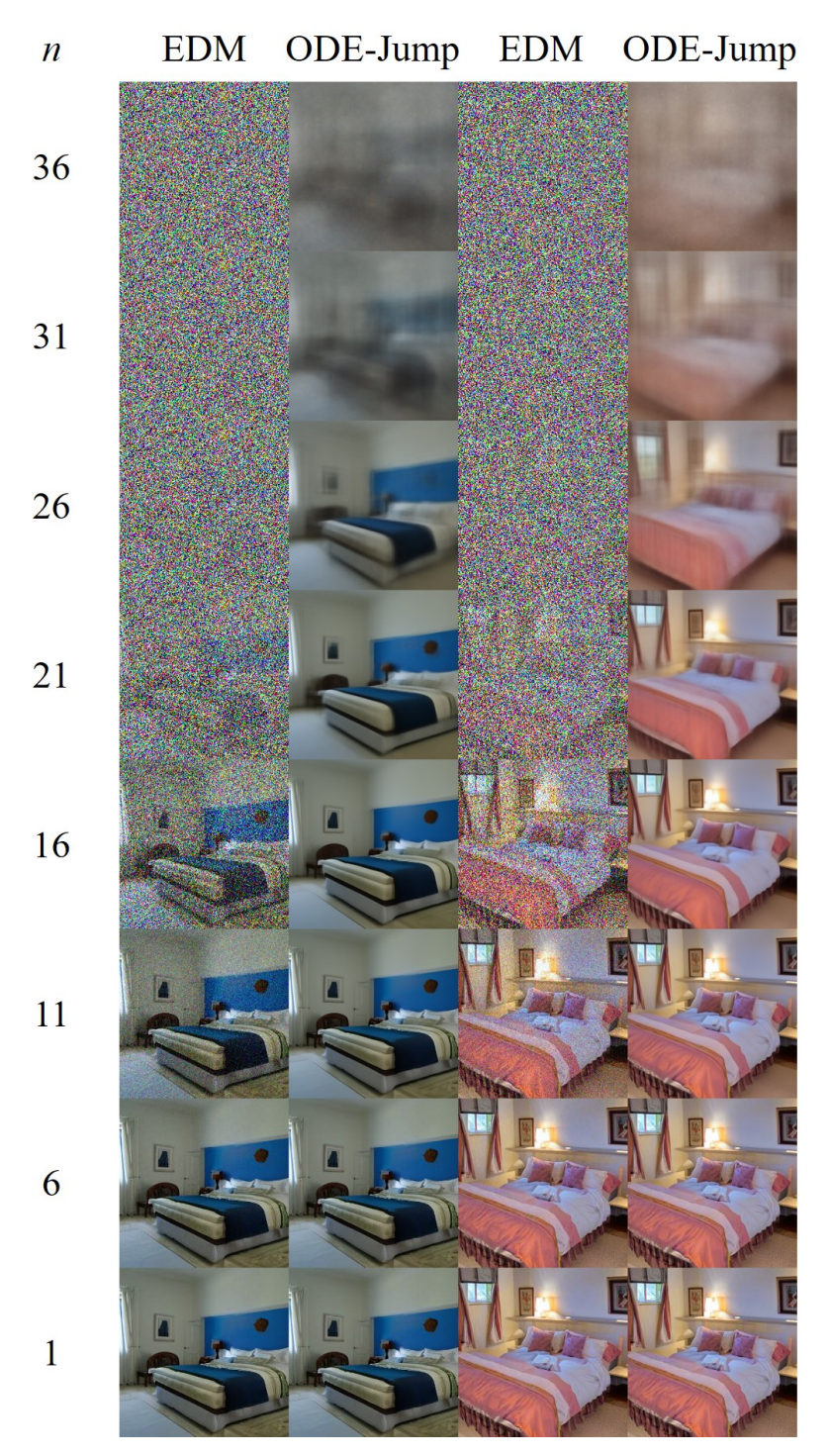


Figure 14: The visual comparison of EDM and ODE-Jump on LSUN Bedroom (detailed version).

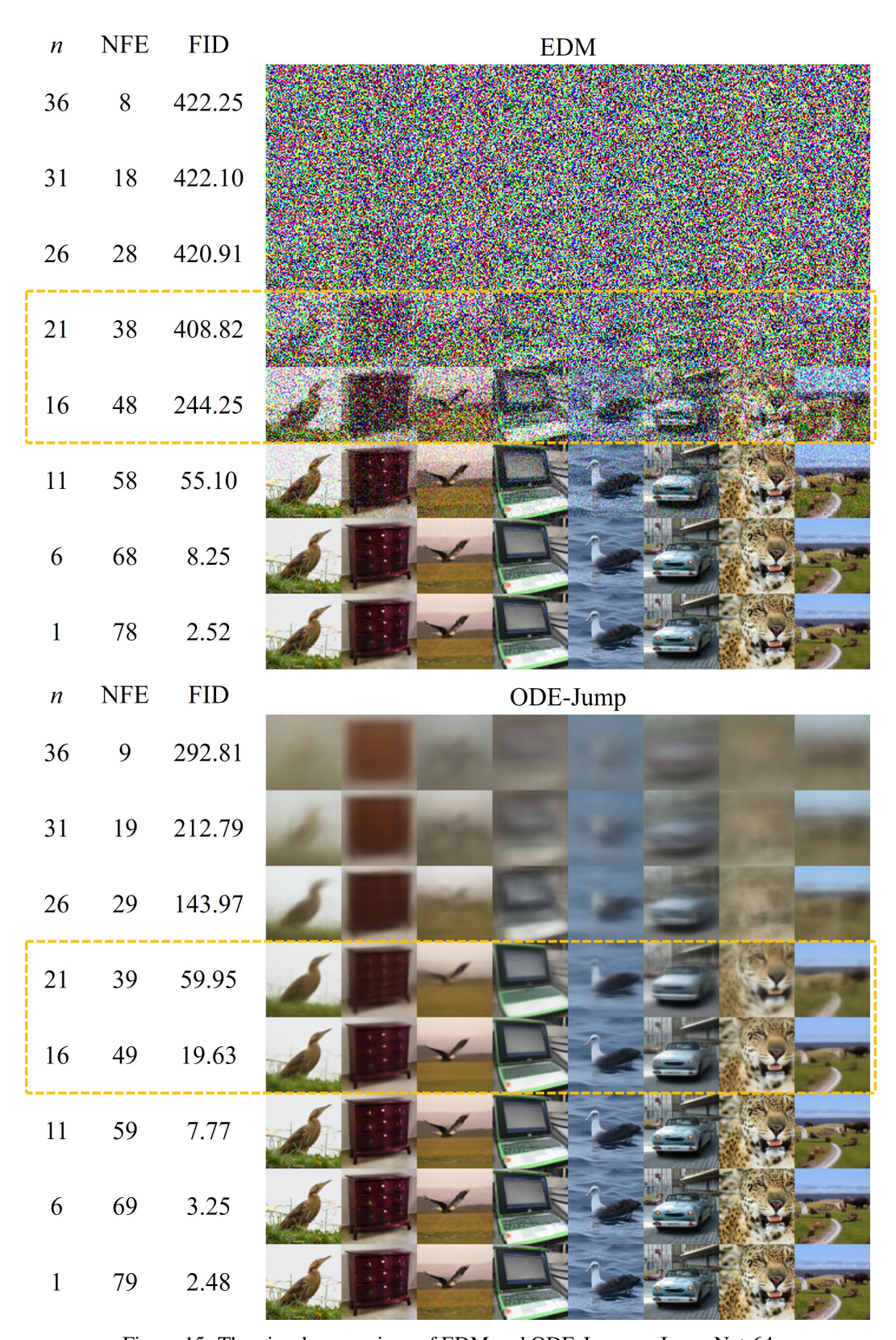


Figure 15: The visual comparison of EDM and ODE-Jump on ImageNet-64.

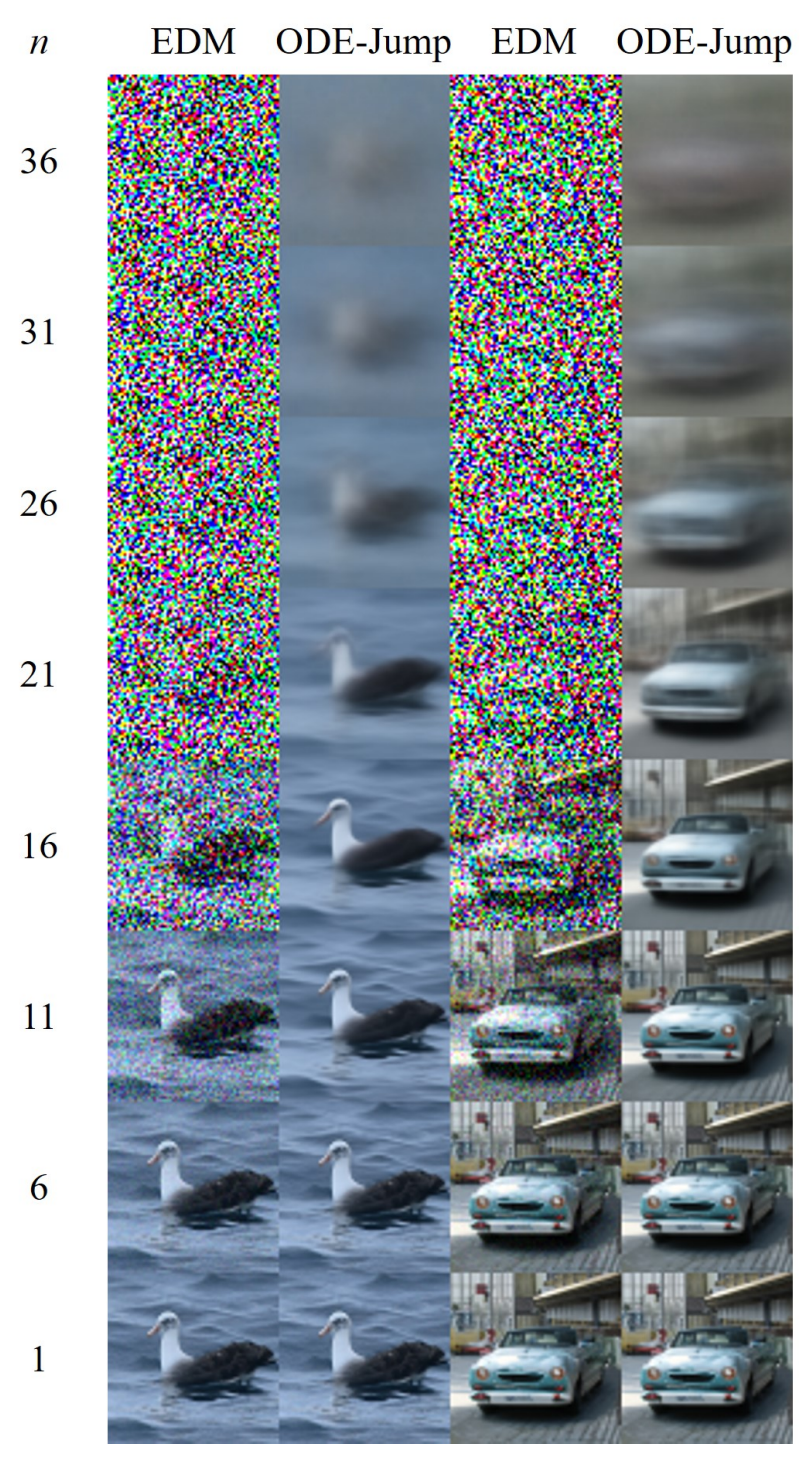


Figure 16: The visual comparison of EDM and ODE-Jump on ImageNet-64 (detailed version).

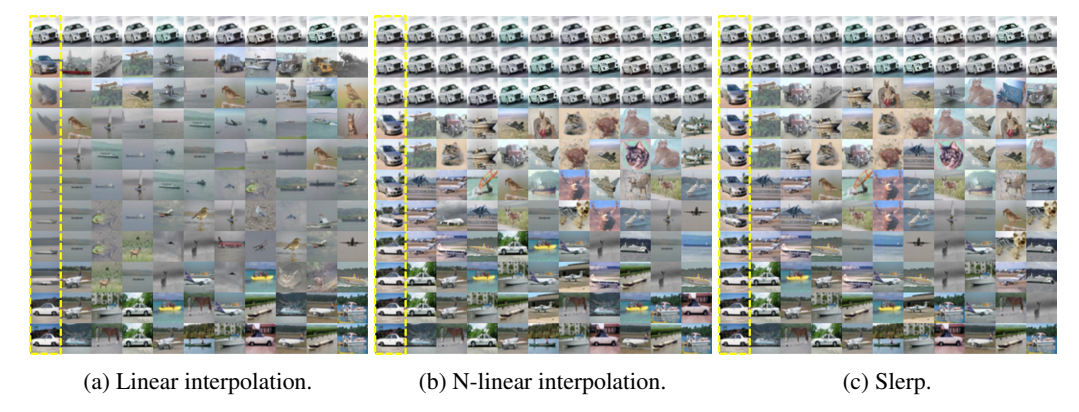


Figure 17: We further calculate the k-nearest neighbors (k=10) of our generated images to the real data, to demonstrate how different modes are smoothly traversed in the latent interpolation process.

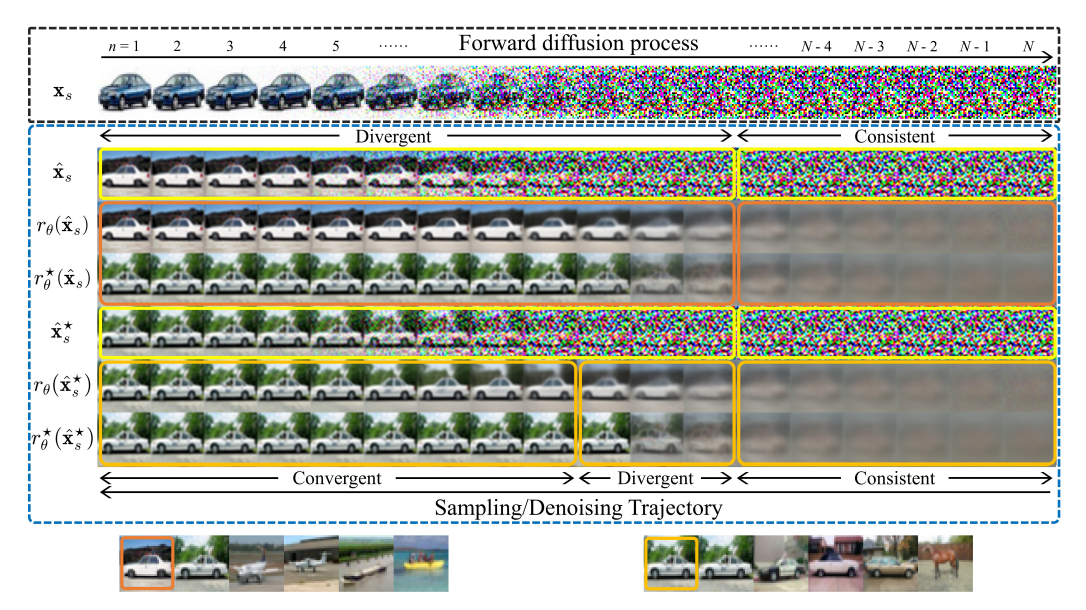


Figure 18: The unconditional generation on CIFAR-10. *Top:* We visualize a forward diffusion process of a randomly-selected image to obtain its encoding $\hat{\mathbf{x}}_{s_N}$ and simulate multiple trajectories starting from this encoding. *Bottom:* The k-nearest neighbor (k=5) of $r_{\boldsymbol{\theta}}(\hat{\mathbf{x}}_{s_1})$ and $r_{\boldsymbol{\theta}}^{\star}(\hat{\mathbf{x}}_{s_1}^{\star})$.

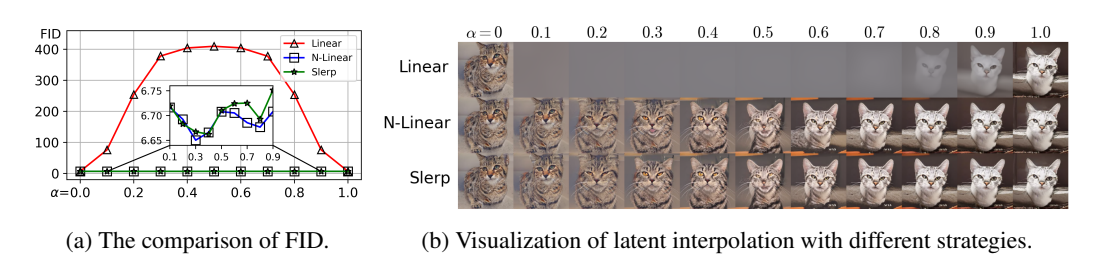


Figure 19: The latent interpolation results on LSUN Cat.

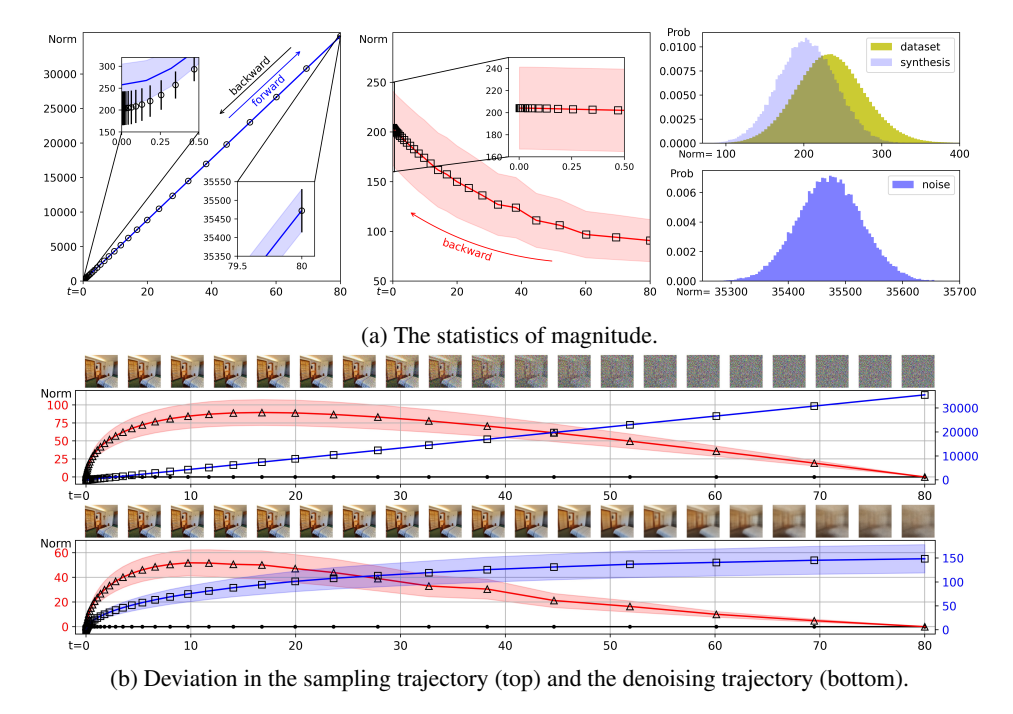


Figure 20: LSUN Bedroom.

A.3 More Results on Other SDEs

In this section, we provide more results with different VE SDE settings on CIFAR-10, including:

- The conditional generation with the checkpoint⁸ of DDPM++ architecture:
 - Trajectory Shape: The results are provided in Figure 22.
 - Diagnosis of Score Deviation: The results are provided in Figure 23.
 - Latent Interpolation: The results are provided in Figure 24.
 - Angle Deviation: The results are provided in Figure 25.

All observations are similar to those of the unconditional case in the main submission.

- The unconditional generation with the checkpoint of NCSN++ architecture:
 - Trajectory Shape: The results are provided in Figure 26. The observations are similar to those of the unconditional generation case in the main submission. An outlier appears at about t=40 and we find that its score deviation becomes abnormally large. This implies the model probably fails to learn a good score direction at this point.

A.4 More Results on the VP-SDE

In this section, we provide the preliminary results with a variance-preserving SDE, following the configurations of EDM [KAAL22] (see Table 1 in their paper). We conduct unconditional generation with the checkpoint ¹⁰ of DDPM++ architecture.

We find that in this case, the data distribution and the noise distribution are still smoothly connected with an explicit, quasi-linear sampling trajectory, and another implicit denoising trajectory. The monotone properties of VE-SDE discussed in Section 3.2 are generally (but not strictly) hold for VP-SDE. Nevertheless, further investigation is required in order to thoroughly understand the behavior of VP-SDE. We leave it for future work.

⁸https://nvlabs-fi-cdn.nvidia.com/edm/pretrained/edm-cifar10-32x32-cond-vp.pkl

⁹https://nvlabs-fi-cdn.nvidia.com/edm/pretrained/edm-cifar10-32x32-uncond-ve.pkl

¹⁰https://nvlabs-fi-cdn.nvidia.com/edm/pretrained/baseline/

baseline-cifar10-32x32-uncond-vp.pkl

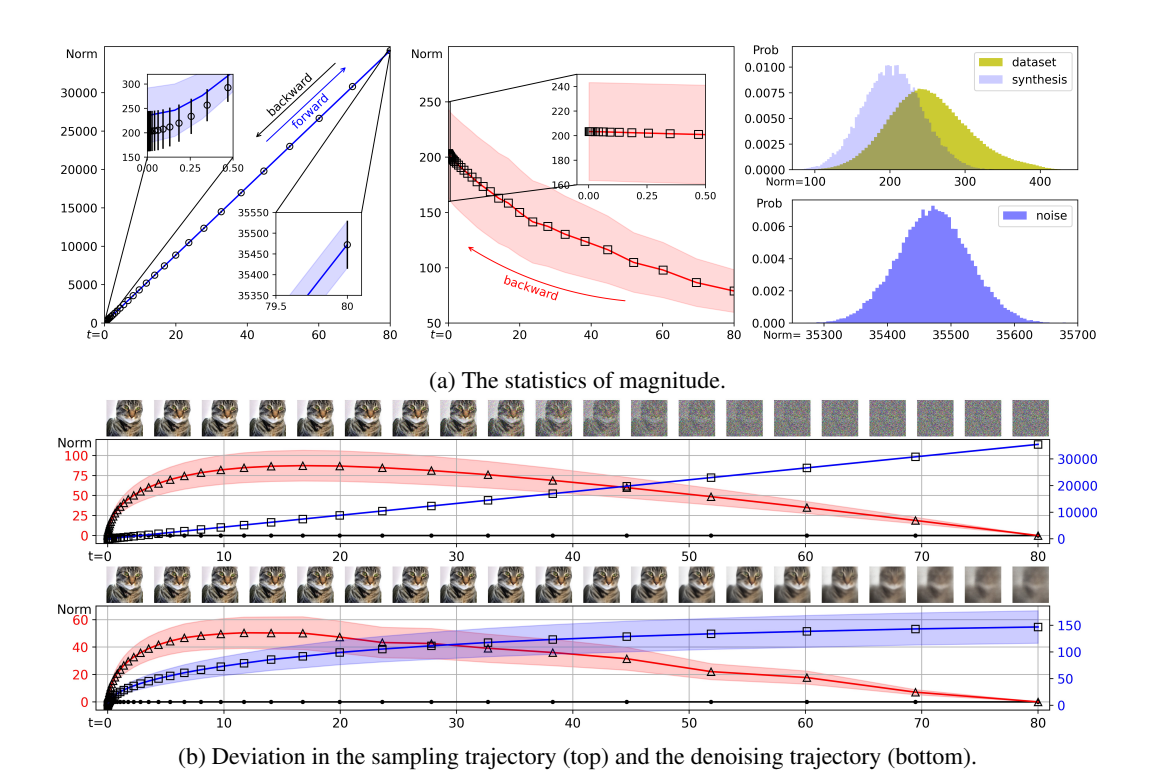


Figure 21: LSUN Cat.

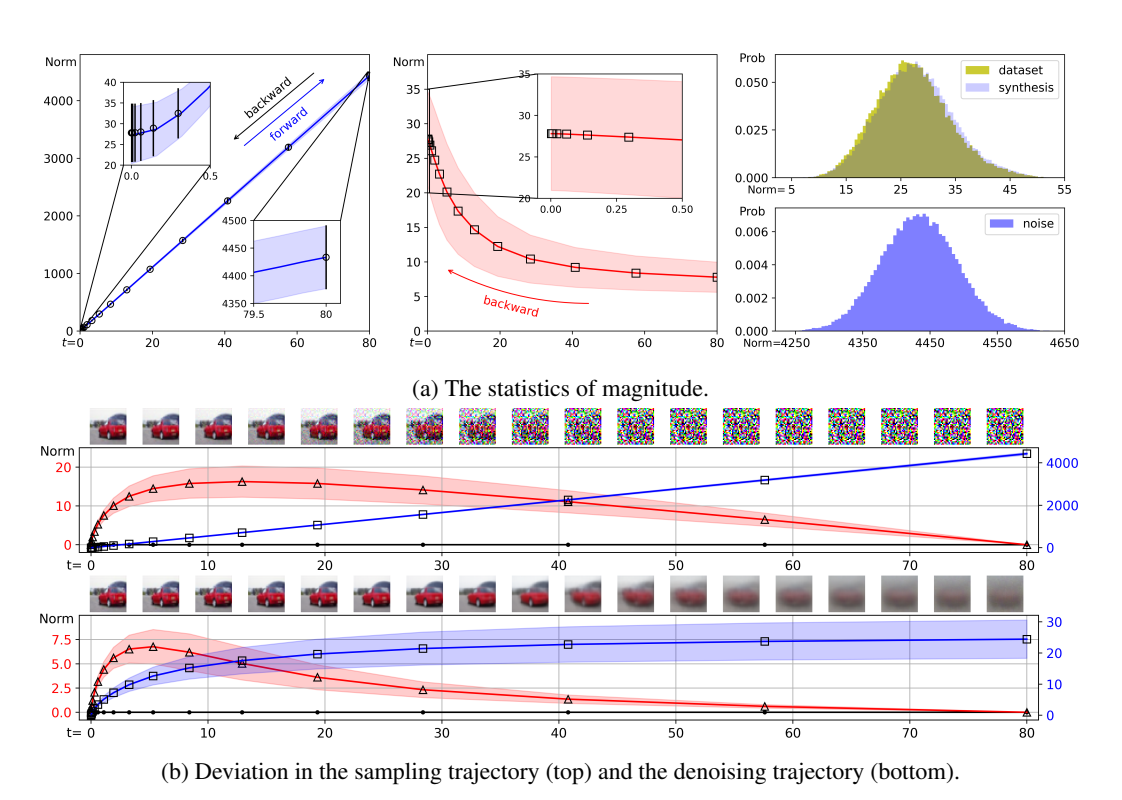


Figure 22: The conditional generation with VE-SDE and DDPM++ architecture.

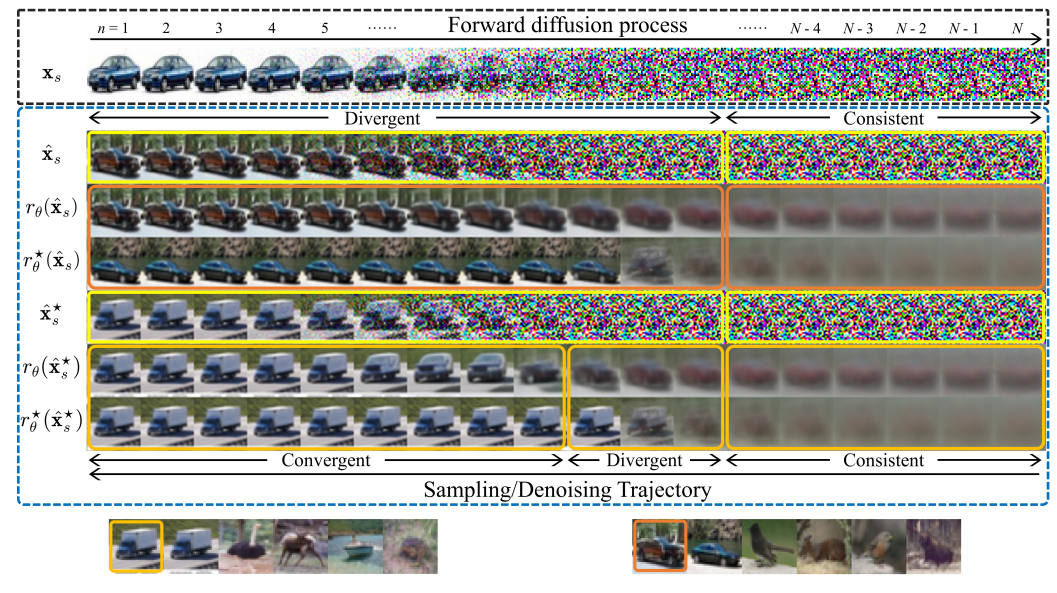


Figure 23: The conditional generation on CIFAR-10. *Top:* We visualize a forward diffusion process of a randomly-selected image to obtain its encoding $\hat{\mathbf{x}}_{s_N}$ and simulate multiple trajectories starting from this encoding. *Bottom:* The k-nearest neighbor (k=5) of $r_{\theta}(\hat{\mathbf{x}}_{s_1})$ and $r_{\theta}^{\star}(\hat{\mathbf{x}}_{s_1}^{\star})$.

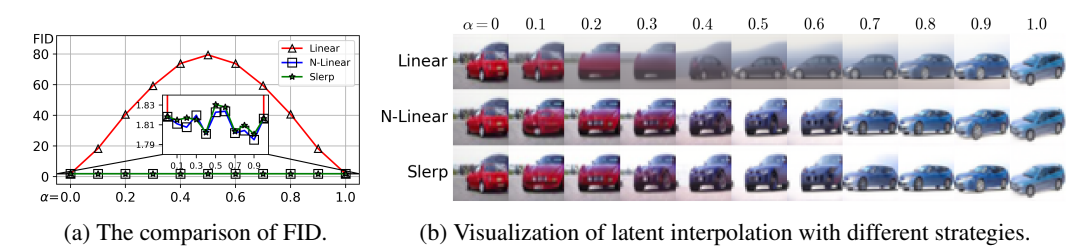


Figure 24: The latent interpolation results on CIFAR-10 with conditional generation.

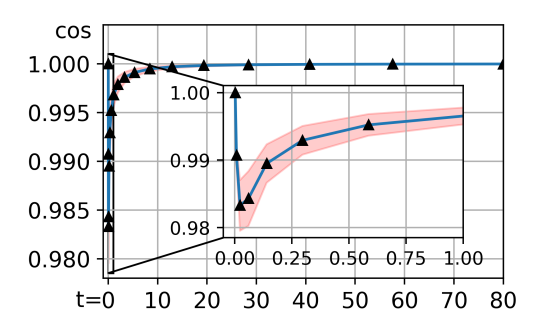


Figure 25: The angle deviation in the sampling trajectory is calculated by the cosine between the backward ODE direction $-\frac{d\mathbf{x}_t}{dt}\big|_s$ and the direction pointing to the final point $(\hat{\mathbf{x}}_{s_0} - \hat{\mathbf{x}}_s)$ at discrete time s. The angle deviation always stays in a narrow range (from about 0.98 to 1.00).

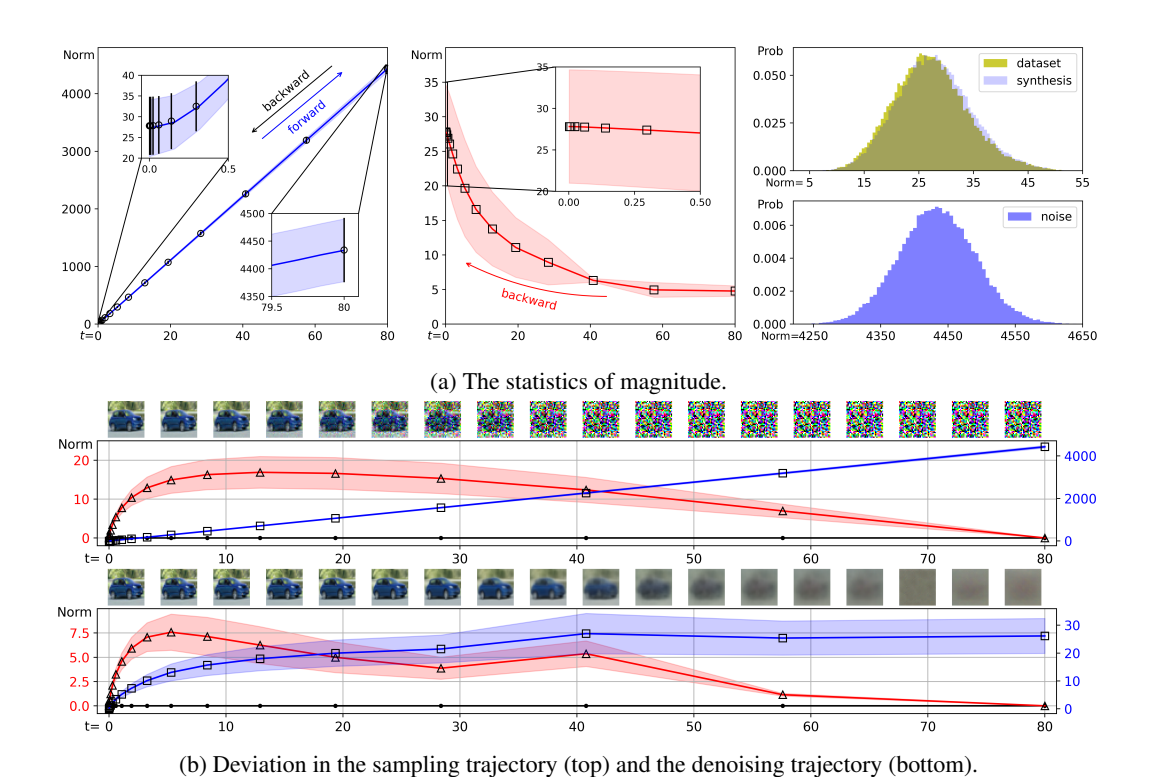


Figure 26: The unconditional generation with VE-SDE and NCSN++ architecture.

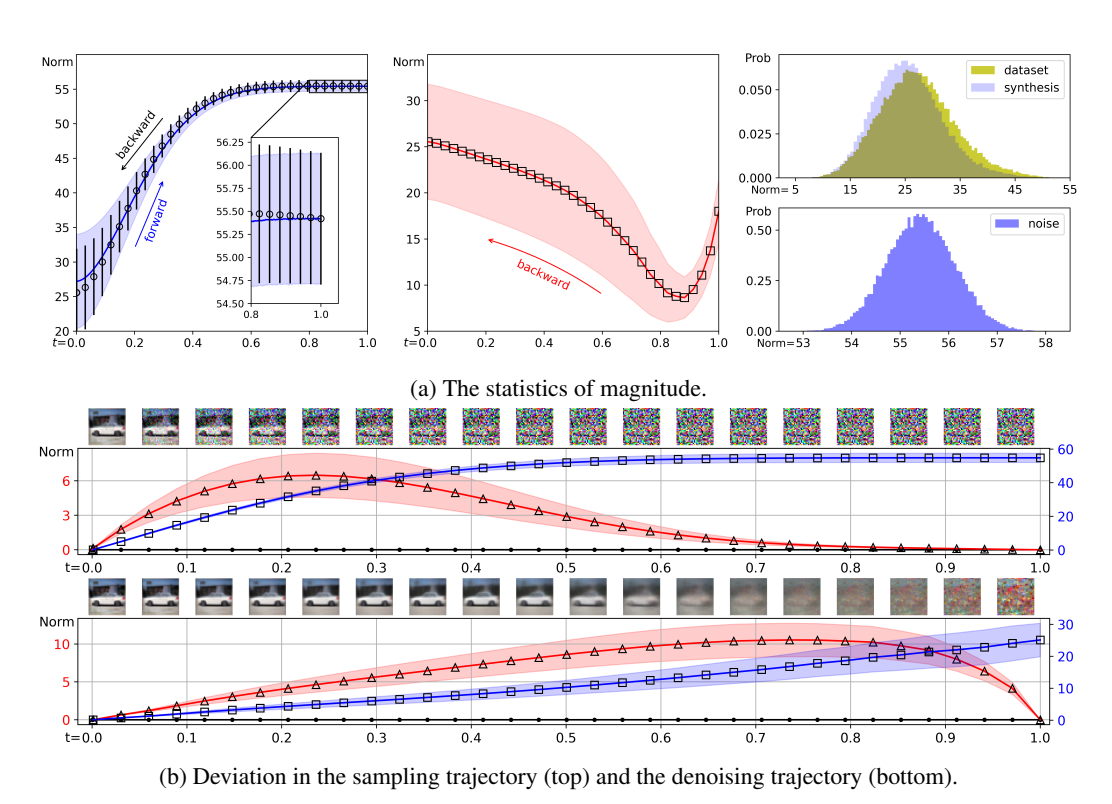


Figure 27: The unconditional generation with VP-SDE and DDPM++ architecture.

B Proofs

B.1 An Empirical Bayes Perspective on the Connection between DSM and DAE

In fact, the deep connection between *denoising autoencoder* (DAE) and *denoising score matching* (DSM) is already existed within the framework of *empirical Bayes*, which was developed more than half a century ago [Rob56]. We next recap the basic concepts of these terminologies [VLBM08, AB14, Vin11, RS11, Efr10, SH19, KAAL22] and discuss how they are interconnected, especially in the common setting of diffusion models (Gaussian kernel density estimation). All theoretical results are followed with the concise proofs for completion.

Suppose that \mathbf{x} is sampled from an underlying data distribution $p_d(\mathbf{x})$, and the corresponding noisy sample $\hat{\mathbf{x}}$ is generated by a Gaussian perturbation kernel $\hat{\mathbf{x}} \sim p_t(\hat{\mathbf{x}}|\mathbf{x}) = \mathcal{N}(\hat{\mathbf{x}}|\mathbf{x}, \sigma_t^2\mathbf{I})$ with an isotropic variance σ_t^2 . We can equivalently denote the noisy sample as $\hat{\mathbf{x}} = \mathbf{x} + \mathbf{z}$ with $\mathbf{z} \sim \mathcal{N}(\mathbf{0}, \sigma_t^2\mathbf{I})$ based on the re-parameterization trick. In diffusion models, we actually have a spectrum of such Gaussian kernels but we just take one of them as an example to simplify the notation.

Lemma 1. The optimal estimator $r_{\theta}^{\star}(\hat{\mathbf{x}}; \sigma_t)$, also known as Bayesian least squares estimator, of the denoising autoencoder (DAE) objective is the conditional expectation $\mathbb{E}(\mathbf{x}|\hat{\mathbf{x}})$

$$\mathcal{L}_{DAE} = \mathbb{E}_{\mathbf{x} \sim p_d(\mathbf{x})} \mathbb{E}_{\mathbf{z} \sim \mathcal{N}(\mathbf{0}, \sigma_t^2 \mathbf{I})} \| r_{\boldsymbol{\theta}} \left(\hat{\mathbf{x}}; \sigma_t \right) - \mathbf{x} \|_2^2$$

$$= \int p_d(\mathbf{x}) p_t(\hat{\mathbf{x}} | \mathbf{x}) \| r_{\boldsymbol{\theta}} \left(\hat{\mathbf{x}}; \sigma_t \right) - \mathbf{x} \|_2^2$$

$$= \int p_t(\hat{\mathbf{x}}) p_t(\mathbf{x} | \hat{\mathbf{x}}) \| r_{\boldsymbol{\theta}} \left(\hat{\mathbf{x}}; \sigma_t \right) - \mathbf{x} \|_2^2.$$
(9)

Proof. The solution of this least squares estimation can be easily obtained by setting the derivative of \mathcal{L}_{DAE} equal to zero. For each noisy sample $\hat{\mathbf{x}}$, we have

$$\nabla_{r_{\theta}(\hat{\mathbf{x}};\sigma_{t})} \mathcal{L}_{\text{DAE}} = \mathbf{0}$$

$$\int p_{t}(\mathbf{x}|\hat{\mathbf{x}}) \left(r_{\theta}^{\star}(\hat{\mathbf{x}};\sigma_{t}) - \mathbf{x}\right) d\mathbf{x} = \mathbf{0}$$

$$\int p_{t}(\mathbf{x}|\hat{\mathbf{x}}) r_{\theta}^{\star}(\hat{\mathbf{x}};\sigma_{t}) d\mathbf{x} = \int p_{t}(\mathbf{x}|\hat{\mathbf{x}}) \mathbf{x} d\mathbf{x}$$

$$r_{\theta}^{\star}(\hat{\mathbf{x}};\sigma_{t}) = \mathbb{E}\left(\mathbf{x}|\hat{\mathbf{x}}\right).$$
(10)

Lemma 2. Given a parametric score function $\nabla_{\hat{\mathbf{x}}} \log p_{\theta,t}(\hat{\mathbf{x}})$ of the marginal distribution $p_t(\hat{\mathbf{x}})$, it will converge to the true score function $\nabla_{\hat{\mathbf{x}}} \log p_t(\hat{\mathbf{x}})$ whether it is trained with the denoising score matching (DSM) objective or the explicit score matching (ESM) objective

$$\mathcal{L}_{\text{DSM}} = \mathbb{E}_{\mathbf{x} \sim p_d(\mathbf{x})} \mathbb{E}_{\mathbf{z} \sim \mathcal{N}(\mathbf{0}, \sigma_t^2 \mathbf{I})} \| \nabla_{\hat{\mathbf{x}}} \log p_{\theta, t}(\hat{\mathbf{x}}) - \nabla_{\hat{\mathbf{x}}} \log p_t(\hat{\mathbf{x}}|\mathbf{x}) \|_2^2$$
(11)

$$\mathcal{L}_{\text{ESM}} = \mathbb{E}_{\hat{\mathbf{x}} \sim p_t(\hat{\mathbf{x}})} \| \nabla_{\hat{\mathbf{x}}} \log p_{\theta,t}(\hat{\mathbf{x}}) - \nabla_{\hat{\mathbf{x}}} \log p_t(\hat{\mathbf{x}}) \|_2^2$$
(12)

Proof. Similar to the Lemma 1, the optimal score function trained with the DSM objective is

$$\nabla_{\hat{\mathbf{x}}} \log p_{\theta,t}^{\star}(\hat{\mathbf{x}}) = \mathbb{E}_{p_{t}(\mathbf{x}|\hat{\mathbf{x}})} \nabla_{\hat{\mathbf{x}}} \log p_{t}(\hat{\mathbf{x}}|\mathbf{x})$$

$$= \int p_{t}(\mathbf{x}|\hat{\mathbf{x}}) \nabla_{\hat{\mathbf{x}}} \log p_{t}(\hat{\mathbf{x}}|\mathbf{x}) d\mathbf{x}$$

$$= \int \frac{p_{d}(\mathbf{x}) p_{t}(\hat{\mathbf{x}}|\mathbf{x})}{p_{t}(\hat{\mathbf{x}})} \nabla_{\hat{\mathbf{x}}} \log p_{t}(\hat{\mathbf{x}}|\mathbf{x}) d\mathbf{x}$$

$$= \int \frac{p_{d}(\mathbf{x})}{p_{t}(\hat{\mathbf{x}})} \nabla_{\hat{\mathbf{x}}} p_{t}(\hat{\mathbf{x}}|\mathbf{x}) d\mathbf{x} = \frac{\nabla_{\hat{\mathbf{x}}} \int p_{d}(\mathbf{x}) p_{t}(\hat{\mathbf{x}}|\mathbf{x}) d\mathbf{x}}{p_{t}(\hat{\mathbf{x}})}$$

$$= \int \frac{p_{d}(\mathbf{x})}{p_{t}(\hat{\mathbf{x}})} \nabla_{\hat{\mathbf{x}}} p_{t}(\hat{\mathbf{x}}|\mathbf{x}) d\mathbf{x} = \frac{\nabla_{\hat{\mathbf{x}}} \int p_{d}(\mathbf{x}) p_{t}(\hat{\mathbf{x}}|\mathbf{x}) d\mathbf{x}}{p_{t}(\hat{\mathbf{x}})}$$

$$= \frac{\nabla_{\hat{\mathbf{x}}} p_{t}(\hat{\mathbf{x}})}{p_{t}(\hat{\mathbf{x}})} = \nabla_{\hat{\mathbf{x}}} \log p_{t}(\hat{\mathbf{x}}).$$
(13)

By setting the derivative of $\mathcal{L}_{\mathrm{ESM}}$ equal to zero, we can also obtain $\nabla_{\hat{\mathbf{x}}} \log p_{\theta,t}^{\star}(\hat{\mathbf{x}}) = \nabla_{\hat{\mathbf{x}}} \log p_t(\hat{\mathbf{x}})$.

Lemma 3. The conditional expectation can be derived from the score function of the marginal distribution $p_t(\hat{\mathbf{x}})$, i.e., $\mathbb{E}(\mathbf{x}|\hat{\mathbf{x}}) = \hat{\mathbf{x}} + \sigma_t^2 \nabla_{\hat{\mathbf{x}}} \log p_t(\hat{\mathbf{x}})$.

Proof.

$$p_{t}(\hat{\mathbf{x}}) = \int p_{d}(\mathbf{x})p_{t}(\hat{\mathbf{x}}|\mathbf{x})d\mathbf{x} = \int \frac{1}{\sqrt{2\pi\sigma_{t}^{2}}} \exp^{-\frac{\|\hat{\mathbf{x}}-\mathbf{x}\|^{2}}{2\sigma_{t}^{2}}} p_{d}(\mathbf{x})d\mathbf{x}$$

$$\sigma_{t}^{2}\nabla_{\hat{\mathbf{x}}}p_{t}(\hat{\mathbf{x}}) = \int (\mathbf{x} - \hat{\mathbf{x}}) \frac{1}{\sqrt{2\pi\sigma_{t}^{2}}} \exp^{-\frac{\|\hat{\mathbf{x}}-\mathbf{x}\|^{2}}{2\sigma_{t}^{2}}} p_{d}(\mathbf{x})d\mathbf{x}$$

$$\sigma_{t}^{2}\nabla_{\hat{\mathbf{x}}}p_{t}(\hat{\mathbf{x}}) = \int \mathbf{x}p_{d}(\mathbf{x})p_{t}(\hat{\mathbf{x}}|\mathbf{x})d\mathbf{x} - \int \hat{\mathbf{x}}p_{d}(\mathbf{x})p_{t}(\hat{\mathbf{x}}|\mathbf{x})d\mathbf{x}$$

$$\sigma_{t}^{2}\nabla_{\hat{\mathbf{x}}}p_{t}(\hat{\mathbf{x}}) = \int \mathbf{x}p_{d}(\mathbf{x})p_{t}(\hat{\mathbf{x}}|\mathbf{x})d\mathbf{x} - \hat{\mathbf{x}}p_{t}(\hat{\mathbf{x}})$$

$$\sigma_{t}^{2}\frac{\nabla_{\hat{\mathbf{x}}}p_{t}(\hat{\mathbf{x}})}{p_{t}(\hat{\mathbf{x}})} = \int \mathbf{x}p_{t}(\mathbf{x}|\hat{\mathbf{x}})d\mathbf{x} - \hat{\mathbf{x}}$$

$$\mathbb{E}(\mathbf{x}|\hat{\mathbf{x}}) = \hat{\mathbf{x}} + \sigma_{t}^{2}\nabla_{\hat{\mathbf{x}}}\log p_{t}(\hat{\mathbf{x}}).$$
(14)

Remark 1. The above intriguing connection implies that we can obtain the posterior expectation $\mathbb{E}(\mathbf{x}|\hat{\mathbf{x}}) = \int \mathbf{x} p_t(\mathbf{x}|\hat{\mathbf{x}}) d\mathbf{x}$ without explicit accessing to the data density $p_d(\mathbf{x})$ (prior distribution).

Remark 2. Furthermore, we can estimate the marginal distribution $p_t(\hat{\mathbf{x}})$ or its score function $\nabla_{\hat{\mathbf{x}}} \log p_t(\hat{\mathbf{x}})$ from a set of observed noisy samples to approximate the posterior expectation $\mathbb{E}(\mathbf{x}|\hat{\mathbf{x}})$, or say the optimal denoising output $r_{\theta}^{\star}(\hat{\mathbf{x}}; \sigma_t)$. This exactly shares the philosophy of empirical Bayes that learns a Bayesian prior distribution from the observed data to help statistical inference.

We provide a brief overview of empirical Bayes as follows.

In contrast to the standard Bayesian methods that specify a *prior* (such as Gaussian, or non-informative distribution) before observing any data, empirical Bayes methods advocate estimating the prior *empirically* from the data itself, whether in a non-parametric or parametric way [Rob56, Mor83, Efr10]. Using Bayes' theorem, the prior is then converted into the *posterior* by incorporating a *likelihood function* calculated in light of the observed data, as the standard Bayesian methods do.

Remark 3. Learning the marginal distribution $p_t(\hat{\mathbf{x}})$ in Lemma 3 from the observed data is termed as f-modeling in the empirical Bayes literature, in contrast to g-modeling that learns the prior distribution $p_d(\mathbf{x})$ from the observed data, see Chapter 21 of a book for more details [EH16].

Proposition 7. The denoising autoencoder (DAE) objective equals to the denoising score matching (DSM) objective, up to a scaling factor (squared variance), i.e., $\mathcal{L}_{DAE} = \sigma_t^4 \mathcal{L}_{DSM}$.

Proof.

$$\mathcal{L}_{\text{DAE}} = \mathbb{E}_{\mathbf{x} \sim p_d} \mathbb{E}_{\mathbf{z} \sim \mathcal{N}(\mathbf{0}, \sigma_t^2 \mathbf{I})} \| r_{\boldsymbol{\theta}} \left(\hat{\mathbf{x}}; \sigma_t \right) - \mathbf{x} \|_2^2$$

$$= \mathbb{E}_{\mathbf{x} \sim p_d} \mathbb{E}_{\mathbf{z} \sim \mathcal{N}(\mathbf{0}, \sigma_t^2 \mathbf{I})} \| \hat{\mathbf{x}} + \sigma_t^2 \nabla_{\hat{\mathbf{x}}} \log p_{\theta, t} (\hat{\mathbf{x}}) - \mathbf{x} \|_2^2$$

$$= \sigma_t^4 \mathbb{E}_{\mathbf{x} \sim p_d} \mathbb{E}_{\mathbf{z} \sim \mathcal{N}(\mathbf{0}, \sigma_t^2 \mathbf{I})} \| \nabla_{\hat{\mathbf{x}}} \log p_{\theta, t} (\hat{\mathbf{x}}) + \frac{\hat{\mathbf{x}} - \mathbf{x}}{\sigma_t^2} \|_2^2$$

$$= \sigma_t^4 \mathbb{E}_{\mathbf{x} \sim p_d} \mathbb{E}_{\mathbf{z} \sim \mathcal{N}(\mathbf{0}, \sigma_t^2 \mathbf{I})} \| \nabla_{\hat{\mathbf{x}}} \log p_{\theta, t} (\hat{\mathbf{x}}) - \nabla_{\mathbf{x}} \log p_t (\hat{\mathbf{x}} | \mathbf{x}) \|_2^2$$

$$= \sigma_t^4 \mathcal{L}_{\text{DSM}}.$$
(15)

where we adopt $\hat{\mathbf{x}} + \sigma_t^2 \nabla_{\hat{\mathbf{x}}} \log p_{\theta,t}(\hat{\mathbf{x}})$ as a parametric empirical Bayes estimator to $\mathbb{E}(\mathbf{x}|\hat{\mathbf{x}})$, which can be compactly written as $r_{\theta}(\hat{\mathbf{x}}; \sigma_t)$. We have $r_{\theta}(\hat{\mathbf{x}}; \sigma_t) \to r_{\theta}^{\star}(\hat{\mathbf{x}}; \sigma_t)$ as soon as $\nabla_{\hat{\mathbf{x}}} \log p_{\theta,t}(\hat{\mathbf{x}}) \to \nabla_{\hat{\mathbf{x}}} \log p_{\theta,t}^{\star}(\hat{\mathbf{x}}) = \nabla_{\hat{\mathbf{x}}} \log p_{t}(\hat{\mathbf{x}})$, and vice versa.

Remark 4. The relationship between denoising autoencoder (DAE), denoising score matching (DSM), and empirical Bayes are summarized as

$$\underbrace{r_{\boldsymbol{\theta}}\left(\hat{\mathbf{x}}; \sigma_{t}\right) \rightarrow r_{\boldsymbol{\theta}}^{\star}\left(\hat{\mathbf{x}}; \sigma_{t}\right) = \underbrace{\mathbb{E}\left(\mathbf{x}|\hat{\mathbf{x}}\right)}_{\text{DAE}} = \underbrace{\hat{\mathbf{x}} + \sigma_{t}^{2} \nabla_{\hat{\mathbf{x}}} \log p_{t}(\hat{\mathbf{x}}) \leftarrow \hat{\mathbf{x}} + \sigma_{t}^{2} \nabla_{\hat{\mathbf{x}}} \log p_{\theta, t}(\hat{\mathbf{x}})}_{\text{DSM}}$$
(16)

B.2 Magnitude Expansion Property (Proposition 1 in the main submission)

Proposition 1. Given a high-dimensional vector $\mathbf{x} \in \mathbb{R}^d$ and an isotropic Gaussian noise $\mathbf{z} \sim \mathbb{N}\left(\mathbf{0}; \sigma^2 \mathbf{I}_d\right)$, $\sigma > 0$, we have $\mathbb{E} \|\mathbf{z}\|^2 = \sigma^2 d$, and with high probability, \mathbf{z} stays within a "thin shell": $\|\mathbf{z}\| = \sigma \sqrt{d} \pm O(1)$. Additionally, $\mathbb{E}\left[\|\mathbf{x} + \mathbf{z}\|^2 - \|\mathbf{x}\|^2\right] = \sigma^2 d$, $\lim_{d \to \infty} \mathbb{P}\left(\|\mathbf{x} + \mathbf{z}\| > \|\mathbf{x}\|\right) = 1$.

Proof. We denote \mathbf{z}_i as the *i*-th dimension of random variable \mathbf{z} , then the expectation and variance is $\mathbb{E}\left[\mathbf{z}_i\right] = 0$, $\mathbb{V}\left[\mathbf{z}_i\right] = \sigma^2$, respectively. The fourth central moment is $\mathbb{E}\left[\mathbf{z}_i^4\right] = 3\sigma^4$. Additionally,

$$\mathbb{E}\left[\mathbf{z}_{i}^{2}\right] = \mathbb{V}\left[\mathbf{z}_{i}\right] + \mathbb{E}\left[\mathbf{z}_{i}\right]^{2} = \sigma^{2}, \qquad \mathbb{E}\left[\|\mathbf{z}\|^{2}\right] = \mathbb{E}\left[\sum_{i=1}^{d} \mathbf{z}_{i}^{2}\right] = \sum_{i=1}^{d} \mathbb{E}\left[\mathbf{z}_{i}^{2}\right] = \sigma^{2}d,$$

$$\mathbb{V}\left[\|\mathbf{z}\|^{2}\right] = \mathbb{E}\left[\|\mathbf{z}\|^{4}\right] - \left(\mathbb{E}\left[\|\mathbf{z}\|^{2}\right]\right)^{2} = \mathbb{E}\left[\left(\sum_{i=1}^{d} \mathbf{z}_{i}^{2}\right)^{2}\right] - d^{2}\sigma^{4}$$

$$= d \cdot \mathbb{E}\left[\mathbf{z}_{1}^{4} + \mathbf{z}_{1}^{2}\left(\sum_{i=2}^{d} \mathbf{z}_{i}^{2}\right)\right] - d^{2}\sigma^{4}$$

$$= 3d\sigma^{4} + d\left(d - 1\right)\sigma^{4} - d^{2}\sigma^{4} = 2d\sigma^{4},$$
(17)

Then, we have

$$\mathbb{E}\left[\|\mathbf{x} + \mathbf{z}\|^2 - \|\mathbf{x}\|^2\right] = \mathbb{E}\left[\|\mathbf{x}\|^2 + \|\mathbf{z}\|^2 + 2\mathbf{x}^T\mathbf{z} - \|\mathbf{x}\|^2\right]$$

$$= \mathbb{E}\left[\|\mathbf{z}\|^2 + 2\mathbf{x}^T\mathbf{z}\right] = \mathbb{E}\left[\|\mathbf{z}\|^2\right]$$

$$= \sigma^2 d.$$
(18)

Furthermore, the standard deviation of $\|\mathbf{z}\|^2$ is $\sigma^2 \sqrt{2d}$, which means

$$\|\mathbf{z}\|^2 = \sigma^2 d \pm \sigma^2 \sqrt{2d} = \sigma^2 d \pm O\left(\sqrt{d}\right), \qquad \|\mathbf{z}\| = \sigma\sqrt{d} \pm O\left(1\right),$$
 (19)

holds with high probability. In fact, we can bound the sub-gaussian tail as follows

$$\mathbb{P}\left(|\|\mathbf{z}\| - \sigma\sqrt{n}| \ge t\right) \le 2\exp\left(-ct^2\right), \quad \forall t \ge 0,\tag{20}$$

where c is an absolute constant. This property indicates that the magnitude of Gaussian random variable distributes very close to the sphere of radius $\sigma\sqrt{n}$ in the high-dimensional case.

Suppose $t = \sigma \sqrt{d} - 2\|\mathbf{x}\| > 0$, we have

Thus, $\lim_{d\to\infty} \mathbb{P}\left(\|\mathbf{x} + \mathbf{z}\| > \|\mathbf{x}\|\right) = 1$.

$$\underbrace{\mathbb{P}\left(\|\mathbf{x} + \mathbf{z}\| \le \|\mathbf{x}\|\right) < \mathbb{P}\left(\|\mathbf{z}\| - \sigma\sqrt{d}| \ge \sigma\sqrt{d} - 2\|\mathbf{x}\|\right)}_{\text{See Figure 28}} \le 2\exp\left(-c\left(\sigma\sqrt{d} - 2\|\mathbf{x}\|\right)^{2}\right),$$

$$\lim_{d \to \infty} \mathbb{P}\left(\|\mathbf{x} + \mathbf{z}\| \le \|\mathbf{x}\|\right) < \lim_{d \to \infty} 2\exp\left(-c\left(\sigma\sqrt{d} - 2\|\mathbf{x}\|\right)^{2}\right) = 0.$$
(21)

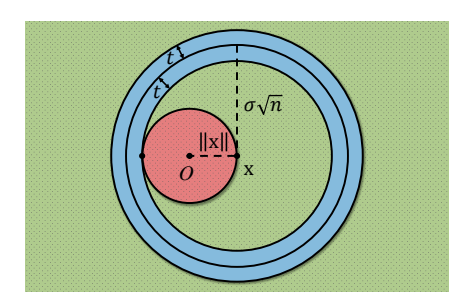


Figure 28: A simple geometric illustration (the green region is bigger than the red region).

B.3 The Optimal Denoising Output

Suppose we have a training dataset $\mathcal{D} = \{\mathbf{x}_i\}_{i=1}^N$ where each data \mathbf{x}_i is sampled from an unknown data distribution $p_d(\mathbf{x})$, and the corresponding noisy counterpart $\hat{\mathbf{x}}_i$ is generated by a Gaussian perturbation kernel $\hat{\mathbf{x}} \sim p_t(\hat{\mathbf{x}}|\mathbf{x}) = \mathcal{N}(\hat{\mathbf{x}}|\mathbf{x}, \sigma_t^2\mathbf{I})$ with an isotropic variance σ_t^2 . The empirical data distribution $p_\delta(\mathbf{x})$ is denoted as a summation of multiple *Dirac delta functions*: $p_\delta(\mathbf{x}) = \frac{1}{N} \sum_{i=1}^N \delta(\|\mathbf{x} - \mathbf{x}_i\|)$, and the Gaussian kernel density estimation is

$$p_t(\hat{\mathbf{x}}) = \int p_t(\hat{\mathbf{x}}|\mathbf{x}) p_{\delta}(\mathbf{x}) = \frac{1}{N} \sum_i \mathcal{N}\left(\hat{\mathbf{x}}; \mathbf{x}_i, \sigma_t^2 \mathbf{I}\right).$$
 (22)

Based on Lemma 1 and 3, the optimal denoising output is

$$r_{\boldsymbol{\theta}}^{\star}(\hat{\mathbf{x}}; \sigma_{t}) = \mathbb{E}\left(\mathbf{x}|\hat{\mathbf{x}}\right) = \hat{\mathbf{x}} + \sigma_{t}^{2} \nabla_{\hat{\mathbf{x}}} \log p_{t}(\hat{\mathbf{x}})$$

$$= \hat{\mathbf{x}} + \sigma_{t}^{2} \sum_{i} \frac{\nabla_{\hat{\mathbf{x}}} \mathcal{N}\left(\hat{\mathbf{x}}; \mathbf{x}_{i}, \sigma_{t}^{2} \mathbf{I}\right)}{\sum_{j} \mathcal{N}\left(\hat{\mathbf{x}}; \mathbf{x}_{j}, \sigma_{t}^{2} \mathbf{I}\right)}$$

$$= \hat{\mathbf{x}} + \sigma_{t}^{2} \sum_{i} \frac{\mathcal{N}\left(\hat{\mathbf{x}}; \mathbf{x}_{i}, \sigma_{t}^{2} \mathbf{I}\right)}{\sum_{j} \mathcal{N}\left(\hat{\mathbf{x}}; \mathbf{x}_{j}, \sigma_{t}^{2} \mathbf{I}\right)} \left(\frac{\mathbf{x}_{i} - \hat{\mathbf{x}}}{\sigma_{t}^{2}}\right)$$

$$= \hat{\mathbf{x}} + \sum_{i} \frac{\mathcal{N}\left(\hat{\mathbf{x}}; \mathbf{x}_{i}, \sigma_{t}^{2} \mathbf{I}\right)}{\sum_{j} \mathcal{N}\left(\hat{\mathbf{x}}; \mathbf{x}_{j}, \sigma_{t}^{2} \mathbf{I}\right)} \left(\mathbf{x}_{i} - \hat{\mathbf{x}}\right)$$

$$= \sum_{i} \frac{\mathcal{N}\left(\hat{\mathbf{x}}; \mathbf{x}_{i}, \sigma_{t}^{2} \mathbf{I}\right)}{\sum_{j} \mathcal{N}\left(\hat{\mathbf{x}}; \mathbf{x}_{j}, \sigma_{t}^{2} \mathbf{I}\right)} \mathbf{x}_{i}$$

$$= \sum_{i} \frac{\exp\left(-\|\hat{\mathbf{x}} - \mathbf{x}_{i}\|^{2} / 2\sigma_{t}^{2}\right)}{\sum_{j} \exp\left(-\|\hat{\mathbf{x}} - \mathbf{x}_{j}\|^{2} / 2\sigma_{t}^{2}\right)} \mathbf{x}_{i}.$$
(23)

This equation appears to be highly similar to the classic non-parametric mean shift [FH75, Che95, CM02], especially annealed mean shift [SBvdH05]. The detailed discussion is provided in Section 4.

B.4 Time-Schedule Function

We denote a monotone increasing *time-schedule function* as $\log s(i):[1,N]\to\mathbb{R}$ that satisfies $s(1)=\sigma_{\min}, s(N)=\sigma_{\max}$. Typical examples include:

- Linear function: $s(i) = \sigma_{\min} + \frac{i-1}{N-1}(\sigma_{\max} \sigma_{\min})$,
- Quadratic function: $s(i) = \sigma_{\min} + \left(\frac{i-1}{N-1}\right)^2 (\sigma_{\max} \sigma_{\min}),$
- Polynomial function: $s(i) = \left(\sigma_{\min}^{1/\rho} + \frac{i-1}{N-1}\left(\sigma_{\max}^{1/\rho} \sigma_{\min}^{1/\rho}\right)\right)^{\rho}$.

The (backward) numerical differentiation $\log s(\cdot)$ at discrete timestamp n+1 ($n \in \mathbb{Z}^+$) is

$$\frac{\partial \log s(i)}{\partial i}\Big|_{n+1} \approx \log s(n+1) - \log s(n)$$

$$= \log \frac{s(n+1)}{s(n)} = -\log \frac{s(n)}{s(n+1)}$$

$$\approx 1 - \frac{s(n)}{s(n+1)}$$

$$= \frac{s(n+1) - s(n)}{s(n+1)} \stackrel{\text{def}}{=} w(n) \in (0,1),$$
(24)

where the approximation error disappears as $N \to \infty$. w(n) is exactly the convex combination factor of the annealed mean shift iteration (denoising output) and the current position to determine the next position in a numerical Euler step (see Figure 29). In this sense, various time-schedule functions (such as uniform, quadratic, polynomial [SE19, SME21, KAAL22]) essentially boil down

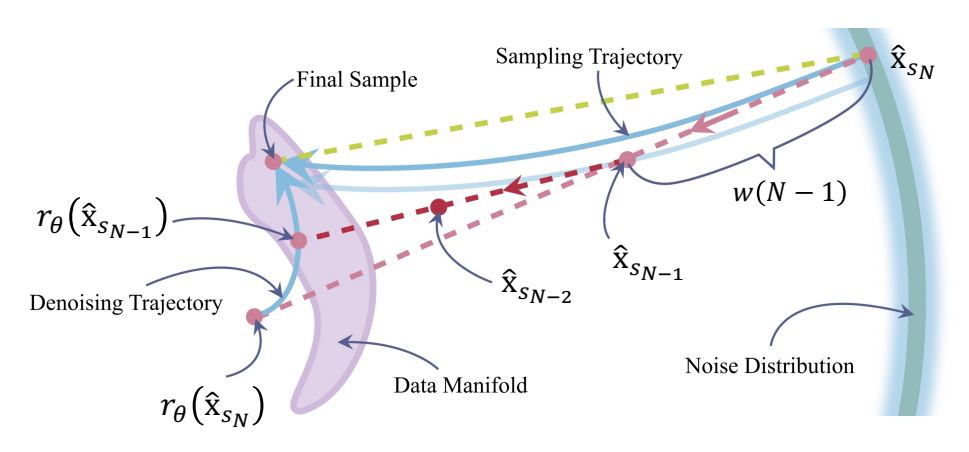


Figure 29: The annealed mean shift iteration (denoising output) and the current position are convexly combined to determine the next position in a numerical Euler step.

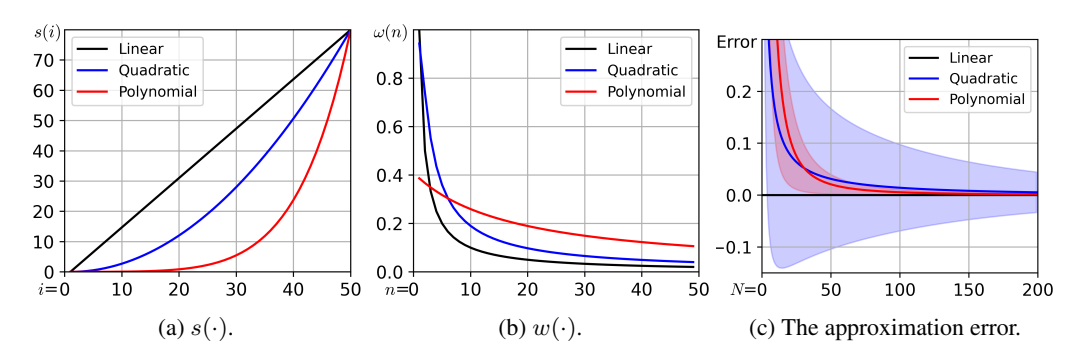


Figure 30: The comparison of time-schedule functions.

to different weighting functions (w(n)), as shown in Figure 30. Therefore, we can learn a parametric neural network $w_{\phi}(n) = \zeta(s_{\phi}(n))$ with the sigmoid function $\zeta(x) = \frac{\exp(x)}{\exp(x)+1}$ to adaptively assign a proper weight for better visual quality. This is similar to the learning of noise schedule function in [KSPH21].

B.5 In-Distribution Latent Interpolation

Given two independent latent encodings, $\hat{\mathbf{x}}_{s_N}^{(1)}$, $\hat{\mathbf{x}}_{s_N}^{(2)} \sim \mathcal{N}(\mathbf{0}, T^2\mathbf{I})$, and $0 < \alpha < 1$, we have three latent interpolation strategies as follows and their comparison is provided in Table 1.

• linear interpolation:

$$\hat{\mathbf{x}}_{s_N}^{(\alpha)} = (1 - \alpha)\hat{\mathbf{x}}_{s_N}^{(1)} + \alpha\hat{\mathbf{x}}_{s_N}^{(2)}; \tag{25}$$

• spherical linear interpolation (slerp):

$$\hat{\mathbf{x}}_{s_N}^{(\alpha)} = \frac{\sin[(1-\alpha)\psi]}{\sin(\psi)} \hat{\mathbf{x}}_{s_N}^{(1)} + \frac{\sin(\alpha\psi)}{\sin(\psi)} \hat{\mathbf{x}}_{s_N}^{(2)}, \quad \psi = \arccos\left(\frac{\langle \hat{\mathbf{x}}_{s_N}^{(1)}, \hat{\mathbf{x}}_{s_N}^{(2)} \rangle}{\|\hat{\mathbf{x}}_{s_N}^{(1)}\|_2 \cdot \|\hat{\mathbf{x}}_{s_N}^{(2)}\|_2}\right), \quad (26)$$

where ψ is calculated as the angle subtended by the arc connecting two encodings;

• in-distribution interpolation:

$$\hat{\mathbf{x}}_{s_N}^{(\lambda)} = \sqrt{(1-\lambda^2)}\hat{\mathbf{x}}_{s_N}^{(1)} + \lambda\hat{\mathbf{x}}_{s_N}^{(2)}.$$
 (27)

In particular, by setting $\lambda = \alpha/\sqrt{\alpha^2 + (1-\alpha^2)}$, we obtain

• normalized linear interpolation (n-linear):

$$\hat{\mathbf{x}}_{s_N}^{(\alpha)} = \frac{\sqrt{1 - \alpha^2}}{\sqrt{\alpha^2 + (1 - \alpha^2)}} \hat{\mathbf{x}}_{s_N}^{(1)} + \frac{\alpha}{\sqrt{\alpha^2 + (1 - \alpha^2)}} \hat{\mathbf{x}}_{s_N}^{(2)}.$$
 (28)

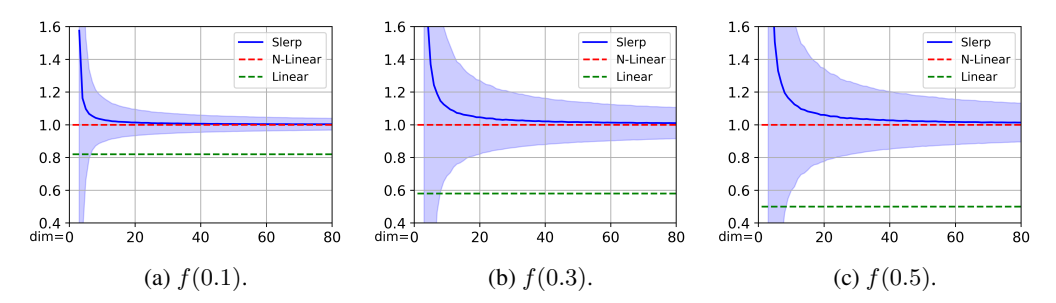


Figure 31: The comparison of three interpolation strategies with different dimensions.

Thanks to the linearity of Gaussian random variable, the interpolated latent encoding by each of the above strategies still belongs to a Gaussian distribution with zero mean. We thus only need to check the variance to see whether the distribution shift happens.

The variance comparison is provided as follows

• linear interpolation:

$$\mathbb{V}\left(\hat{\mathbf{x}}_{s_N}^{(\alpha)}\right) = \mathbb{V}\left((1-\alpha)\hat{\mathbf{x}}_{s_N}^{(1)} + \alpha\hat{\mathbf{x}}_{s_N}^{(2)}\right)
= (1-\alpha)^2 \mathbb{V}\left(\hat{\mathbf{x}}_{s_N}^{(1)}\right) + \alpha^2 \mathbb{V}\left(\hat{\mathbf{x}}_{s_N}^{(2)}\right)
= ((1-\alpha)^2 + \alpha^2) T^2 \mathbf{I} \stackrel{\text{def}}{=} f(\alpha) T^2 \mathbf{I},$$
(29)

where sup $f(\alpha) = 1$ if $\alpha \to 0$ or 1, and min $f(\alpha) = 0.5$ if $\alpha = 0.5$.

• spherical linear interpolation (slerp):

$$\mathbb{V}\left(\hat{\mathbf{x}}_{s_{N}}^{(\alpha)}\right) = \mathbb{V}\left(\frac{\sin[(1-\alpha)\psi]}{\sin(\psi)}\hat{\mathbf{x}}_{s_{N}}^{(1)} + \frac{\sin(\alpha\psi)}{\sin(\psi)}\hat{\mathbf{x}}_{s_{N}}^{(2)}\right) \\
= \frac{\sin^{2}[(1-\alpha)\psi] + \sin^{2}(\alpha\psi)}{\sin^{2}(\psi)}T^{2}\mathbf{I} \stackrel{\text{def}}{=} f(\alpha)T^{2}\mathbf{I},$$
(30)

where
$$f(0.5) = \frac{2\sin^2[\psi/2]}{\sin^2(\psi)} = \frac{1}{2\cos^2(\psi/2)} = 2\sec^2(\psi/2) \ge 0.5$$
.

Since these two latent encodings $\hat{\mathbf{x}}_{s_N}^{(1)}$ and $\hat{\mathbf{x}}_{s_N}^{(2)}$ are almost orthogonal with the angle $\frac{1}{2}\pi+O_p(d^{-0.5})$ in high dimensions [HMN05, Ver18], we can conclude that asymptotically,

$$\lim_{d \to \infty} \mathbb{V}\left(\hat{\mathbf{x}}_{s_N}^{(\alpha)}\right) = \left(\sin^2[(1-\alpha)\frac{\pi}{2}] + \sin^2(\alpha\frac{\pi}{2})\right) T^2 \mathbf{I} = T^2 \mathbf{I},\tag{31}$$

• in-distribution interpolation:

$$\mathbb{V}\left(\hat{\mathbf{x}}_{s_N}^{(\lambda)}\right) = \mathbb{V}\left(\sqrt{(1-\lambda^2)}\hat{\mathbf{x}}_{s_N}^{(1)} + \lambda\hat{\mathbf{x}}_{s_N}^{(2)}\right) = f(\lambda)T^2\mathbf{I} = T^2\mathbf{I}.$$
 (32)

We provide a comparison of three interpolation strategies with different dimensions in Figure 31.

Remark 5. In high dimensions, linear interpolation [HJA20] shifts the latent distribution while spherical linear interpolation [SME21] asymptotically $(d \to \infty)$ maintains the latent distribution.

Remark 6. In-distribution interpolation preserves the latent distribution under interpolation.

Remark 7. If two latent encodings share the same magnitude, i.e., $\|\hat{\mathbf{x}}_{s_N}^{(1)}\|^2 = \|\hat{\mathbf{x}}_{s_N}^{(2)}\|^2 = C^2$, then spherical linear interpolation maintains the magnitude, i.e., $\|\hat{\mathbf{x}}_{s_N}^{(\alpha)}\|^2 = C^2$.

Proof. Since $\sin [(1 - \alpha) \psi] = \sin \psi \cos (\alpha \psi) - \cos \psi \sin (\alpha \psi)$, we have

$$\|\hat{\mathbf{x}}_{s_{N}}^{(\alpha)}\|^{2} = \left\| \frac{\sin\left[(1-\alpha)\psi\right]}{\sin\psi} \hat{\mathbf{x}}_{s_{N}}^{(1)} + \frac{\sin\left(\alpha\psi\right)}{\sin\psi} \hat{\mathbf{x}}_{s_{N}}^{(2)} \right\|^{2}$$

$$= \frac{1}{\sin^{2}\psi} \left(\sin^{2}\left[(1-a)\psi\right] \|\hat{\mathbf{x}}_{s_{N}}^{(1)}\|^{2} + \sin^{2}\left(\alpha\psi\right) \|\hat{\mathbf{x}}_{s_{N}}^{(2)}\|^{2} + 2\sin\left[(1-\alpha)\psi\right] \sin\left(\alpha\psi\right) \left\langle \hat{\mathbf{x}}_{s_{N}}^{(1)}, \hat{\mathbf{x}}_{s_{N}}^{(2)} \right\rangle \right),$$
(33)

Table 1: The comparison of three latent interpolation strategies.

Interpolation	Distribution Shift	Magnitude Shift
Linear Spherical linear In-distribution	(asymptotic) X	× (asymptotic, approximate) ×

where

$$\sin^{2}\left[\left(1-a\right)\psi\right]\|\hat{\mathbf{x}}_{s_{N}}^{(1)}\|^{2} + \sin^{2}\left(\alpha\psi\right)\|\hat{\mathbf{x}}_{s_{N}}^{(2)}\|^{2}
= \left\{\left[\sin^{2}\psi\cos^{2}\left(\alpha\psi\right) + \cos^{2}\psi\sin^{2}\left(\alpha\psi\right) - 2\sin\psi\cos\psi\sin\alpha\psi\cos\alpha\psi\right] + \sin^{2}\left(\alpha\psi\right)\right\}C^{2}
= \left[\sin^{2}\psi + 2\cos^{2}\psi\sin^{2}\left(\alpha\psi\right) - 2\sin\psi\cos\psi\sin\left(\alpha\psi\right)\cos\left(\alpha\psi\right)\right]C^{2}$$
(34)

and

$$2\sin\left[\left(1-\alpha\right)\psi\right]\sin\left(\alpha\psi\right)\left\langle\hat{\mathbf{x}}_{s_{N}}^{(1)},\hat{\mathbf{x}}_{s_{N}}^{(2)}\right\rangle$$

$$=\left[2\sin\psi\sin\left(\alpha\psi\right)\cos\left(\alpha\psi\right)-2\cos\psi\sin^{2}\left(\alpha\psi\right)\right]C^{2}\cos\psi$$

$$=\left[2\sin\psi\cos\psi\sin\left(\alpha\psi\right)\cos\left(\alpha\psi\right)-2\cos^{2}\psi\sin^{2}\left(\alpha\psi\right)\right]C^{2}.$$
(35)

We then substitute Eq. (34) and Eq. (35) into Eq. (33) and obtain $\|\hat{\mathbf{x}}_{s_N}^{(\alpha)}\|^2 = C^2$.

Remark 8. If two latent encodings share the same magnitude, i.e., $\|\hat{\mathbf{x}}_{s_N}^{(1)}\|^2 = \|\hat{\mathbf{x}}_{s_N}^{(2)}\|^2 = C^2$, then linear interpolation shrinks the magnitude, i.e., $\|\hat{\mathbf{x}}_{s_N}^{(\alpha)}\|^2 < C^2$ while in-distribution interpolation approximately preserves the magnitude in high dimensions.

Proof. In high dimensions $(d \gg 1, C = T\sqrt{d} \gg 1), |\langle \hat{\mathbf{x}}_{s_N}^{(1)}, \hat{\mathbf{x}}_{s_N}^{(2)} \rangle| \approx C$ [Ver18]. Then, we have

• linear interpolation:

$$\|\hat{\mathbf{x}}_{s_{N}}^{(\alpha)}\|^{2} = \|(1-\alpha)\hat{\mathbf{x}}_{s_{N}}^{(1)} + \alpha\hat{\mathbf{x}}_{s_{N}}^{(2)}\|^{2}$$

$$= (1-\alpha)^{2}\|\hat{\mathbf{x}}_{s_{N}}^{(1)}\|^{2} + \alpha^{2}\|\hat{\mathbf{x}}_{s_{N}}^{(2)}\|^{2} + 2\alpha(1-\alpha)\langle\hat{\mathbf{x}}_{s_{N}}^{(1)},\hat{\mathbf{x}}_{s_{N}}^{(2)}\rangle$$

$$\approx ((1-\alpha)^{2} + \alpha^{2})C^{2} < C^{2}.$$
(36)

• *in-distribution interpolation:*

$$\|\hat{\mathbf{x}}_{s_{N}}^{(\alpha)}\|^{2} = \|\sqrt{(1-\lambda^{2})}\hat{\mathbf{x}}_{s_{N}}^{(1)} + \lambda\hat{\mathbf{x}}_{s_{N}}^{(2)}\|^{2}$$

$$= (1-\lambda^{2})\|\hat{\mathbf{x}}_{s_{N}}^{(1)}\|^{2} + \lambda^{2}\|\hat{\mathbf{x}}_{s_{N}}^{(2)}\|^{2} + 2\lambda\sqrt{(1-\lambda^{2})}\langle\hat{\mathbf{x}}_{s_{N}}^{(1)},\hat{\mathbf{x}}_{s_{N}}^{(2)}\rangle$$

$$\approx C^{2}.$$
(37)

C Broader Impact

We expect that our geometric perspective and theoretical insight will advance the understanding of score/diffusion-based generative models and further facilitate the development of more powerful large-scale generative models. This may in turn be used to amplify negative societal effects, such as synthesizing and spreading fake images and videos for malicious purposes.